HHS Public Access

Author manuscript

Nat Immunol. Author manuscript; available in PMC 2024 May 31.

Published in final edited form as:

Nat Immunol. 2024 April ; 25(4): 671–681. doi:10.1038/s41590-024-01772-6.

Lupus autoantibodies initiate neuroinflammation sustained by continuous HMGB1:RAGE signaling and reversed by increased LAIR-1 expression

Kaitlin R. Carroll[1,4], **Mark Mizrachi**[1,4], **Sean Simmons**[2], **Bahtiyar Toz**[1], **Czeslawa Kowal**[1], **Jeffrey Wingard**[1], **Nazila Tehrani**[1], **Aida Zarfeshani**[1], **Nina Kello**[3], **Lara El Khoury**[3], **Rachel Weissman-Tsukamoto**[1], **Joshua Z. Levin**[2], **Bruce T. Volpe**[1], **Betty Diamond**[1,✉]

[1]Institute of Molecular Medicine, The Feinstein Institutes for Medical Research, Manhasset, NY, USA.

[2]Stanley Center for Psychiatric Research, Broad Institute of MIT and Harvard, Cambridge, MA, USA.

[3]Northwell Health, Manhasset, NY, USA.

[4]These authors contributed equally: Kaitlin R. Carroll, Mark Mizrachi.

Abstract

Cognitive impairment is a frequent manifestation of neuropsychiatric systemic lupus erythematosus, present in up to 80% of patients and leading to a diminished quality of life. In the present study, we used a model of lupus-like cognitive impairment that is initiated when antibodies that crossreact with excitatory neuronal receptors penetrate the hippocampus, causing immediate, self-limited, excitotoxic death of hippocampal neurons, which is then followed by a significant loss of dendritic complexity in surviving neurons. This injury creates a maladaptive equilibrium that is sustained in mice for at least 1 year. We identified a feedforward loop of microglial activation and microglia-dependent synapse elimination dependent on neuronal secretion of high

✉**Correspondence and requests for materials** should be addressed to Betty Diamond. bdiamond@northwell.edu.

Author contributions

K.R.C., M.M. and S.S. wrote and edited the paper and designed, performed and analyzed experiments. B.T. designed, performed, and analyzed experiments. J.W., A.Z., N.K. and L.E.K. performed and analyzed experiments. N.T. and R.W.T. performed experiments. C.K. designed, performed and analyzed experiments and edited the paper. J.Z.L. designed and analyzed experiments, edited the paper and oversaw the studies. B.T.V. designed, performed and analyzed experiments, edited the paper and oversaw the studies. B.D. designed and analyzed experiments, wrote and edited the paper and oversaw the studies.

Competing interests

The authors declare no competing interests.

Reporting summary

Further information on research design is available in the Nature Portfolio Reporting Summary linked to this article.

Code availability

Customized code can be accessed at https://github.com/seanken/LupusModel.

Additional information

Extended data is available for this paper at https://doi.org/10.1038/s41590-024-01772-6.

Supplementary information The online version contains supplementary material available at https://doi.org/10.1038/s41590-024-01772-6.

Peer review information *Nature Immunology* thanks George Tsokos and the other, anonymous, reviewer(s) for their contribution to the peer review of this work. Primary Handling Editor: N. Bernard, in collaboration with the *Nature Immunology* team.

mobility group box 1 protein (HMGB1) which binds the receptor for advanced glycation end products (RAGE) and leads to microglial secretion of C1q, upregulation of interleukin-10 with consequent downregulation of leukocyte-associated immunoglobulin-like receptor 1 (LAIR-1), an inhibitory receptor for C1q. Treatment with a centrally acting angiotensin-converting enzyme inhibitor or with an angiotensin-receptor blocker restored a healthy equilibrium, microglial quiescence and intact spatial memory.

The autoimmune disease systemic lupus erythematosus (SLE) is characterized by self-reactive antibodies leading to multi-organ system involvement and is frequently associated with neurological symptoms, most commonly cognitive dysfunction, which is a manifestation of SLE in up to 80% of patients and profoundly impacts quality of life[1]. It is noteworthy that cognitive dysfunction can persist in patients with systemically quiescent disease[2,3]. This suggests a chronic, nonresolving neuropathology that is independent of peripheral disease activity. We have developed a model of cognitive dysfunction caused by anti-double-stranded DNA (dsDNA) antibodies crossreactive with the excitatory neuronal *N*-methyl d-aspartate receptor (NMDAR)[4,5]. These antibodies (termed DNRAbs) are present at high titers in approximately 30% of patients with SLE and in a higher percentage of patients with neuropsychiatric SLE (NPSLE)[6]. They have been isolated from brain tissue of patients with SLE[7] and their presence in cerebrospinal fluid (CSF) associates with nonfocal NPSLE symptoms such as cognitive dysfunction[8].

DNRAbs can be induced in nonspontaneously autoimmune mice by immunizing with a peptide mimotope of dsDNA, D/EWD/EYS/G, a consensus sequence shared by the GluN2A and GluN2B subunits of the NMDAR, which is multimerized on a poly(lysine) backbone[4,9]. Lipopolysaccharide (LPS) administered systemically several weeks post-immunization causes a transient increase in permeability in the blood–brain barrier (BBB), allowing circulating immunoglobulin (Ig) to penetrate the hippocampus[4]. DNRAbs, acting as positive allosteric modulators of the NMDAR[10,11], cause excitotoxic death of approximately 20–30% of CA1 pyramidal neurons[4,11]. The remaining neurons secrete HMGB1 (refs. 12,13), a nuclear protein that, when secreted, can bind the NMDAR and potentiate NMDAR activation[12,14], and directly impair neuronal function[15,16]. Cytosolic HMGB1, a precursor to secreted HMGB1, is abundant in the hippocampus of $DNRAb^+$ mice after LPS administration compared with control mice immunized with the poly(lysine) backbone alone and given systemic LPS ($DNRAb^-$ mice)[12]. There is no detectable acute excitotoxicity and significantly less cytosolic HMGB1 in CA1 pyramidal neurons in $DNRAb^-$ mice[12].

Notably, few reactive microglia (based on morphology and CD68 expression[12,17]) are detected in $DNRAb^+$ mice 2 weeks after LPS administration, at which point DNRAbs are no longer detectable in the brain[12]. By 8 weeks post-LPS administration, more reactive microglia, a clear loss of dendritic arborization and impaired spatial memory are observed. This pathology is mediated by microglia and the complement protein C1q and can be prevented or reversed by central nervous system (CNS)-penetrating angiotensin-converting enzyme (ACE) inhibitors[12].

In the present study, we investigate the mechanisms of this sustained inflammatory state and the restoration of a healthy homeostasis by modulation of the renin–angiotensin system.

We have found that neuronal HMGB1 is crucial to the continuous neuroinflammatory state that occurs after DNRAb injury. The HMGB1 receptor RAGE must also be present for microglial activation and loss of dendritic arborization to occur. This inflammatory state can be treated with the BBB-permeable ACE inhibitor captopril or the angiotensin-receptor blocker (ARB) telmisartan, indicating a requirement for angiotensin II- (ATII-) receptor 1 (AT1R) interactions, but microglia must express the inhibitory C1q receptor LAIR-1 for therapeutic efficacy. HMGB1 induces microglia to upregulate both AT1R (*Agtr1a*) and the canonically anti-inflammatory cytokine *Il10*; interleukin-10 (IL-10) suppresses *Lair1* expression in microglia. Thus, the inhibition of ATII/AT1R signaling is able to halt the self-sustaining inflammatory cycle by lifting the suppression of LAIR-1, which enables microglia and neurons to return to a state of quiescence and a healthy homeostasis.

Results

Neuronal HMGB1 induces microglial activation through RAGE

Brain pathology initiated by DNRAb injury is sustained for at least 12 months, the last time point at which DNRAb$^+$ mice have been assessed, demonstrating a persistent state of hippocampal inflammation long past the transient exposure to DNRAbs and the acute damage that they induce (Extended Data Fig. 1) and consistent with the fact that cognitive dysfunction persists independently from peripheral disease flares in SLE[2,3]. We have shown previously that the neurons remaining after DNRAb-mediated injury have abundant cytosolic HMGB1, a chromatin-binding protein that can be secreted by activated, stressed or damaged cells and acts as a damage-associated molecular pattern (DAMP)[18], which can bind to RAGE and carry nucleic acid ligands to endosomal toll-like receptors (TLRs) to activate monocytes and macrophages[19,20]. As the neurons in these mice appeared to have sustained HMGB1 secretion and as HMGB1 can not only activate microglia but also bind the NMDAR and potentiate its activation in neurons[12–14], we hypothesized that this continued neuronal HMGB1 secretion might play a role in the sustained inflammatory phenotype by inducing a reactive microglial state characteristic of DNRAb$^+$ mice[12]. We generated neuronal HMGB1-deficient (*Camk2a*-cre$^+$*Hmgb1*$^{fl/fl}$, termed HMGB1 cKO (conditional knockout)) DNRAb$^+$ mice and HMGB1-sufficient (*Camk2a*-cre$^-$*Hmgb1*$^{fl/fl}$, termed WT (wild-type)) DNRAb$^+$ mice and then assessed microglial activation state, based on an activation scoring system that uses established morphological features spanning those indicative of a quiescent state (highly ramified, with many thin processes) to highly reactive (amoeboid, with very few or no thick processes)[17,21]. The activation score also takes into account expression of the scavenger receptor CD68, which is involved in phagocytic function. Its level of expression corresponds to reactivity and phagocytic activity[17,21]. We observed significantly decreased microglial activation in HMGB1 cKO mice compared with their HMGB1-sufficient counterparts (Fig. 1a,b).

To determine the direct effect of HMGB1 on microglia, we cultured primary microglia in vitro with HMGB1 and observed a dose-dependent increase in messenger RNA (mRNA) expression of genes encoding proinflammatory cytokines (*Tnf*, *Il1b*) and *C1qa* (Fig. 1c), as well as increased secretion of tumor necrosis factor (TNF) and IL-1β (Fig. 1d). HMGB1 also induced interferon-β (IFN-β; *Ifnb1*) mRNA expression as well as IFN-β secretion

(Fig. 1e,f). Ex vivo microglial stimulations were performed using microglia cultured from neonatal mice[22]; however, we observed the same behavior using primary adult microglia, although the adult microglia have a more muted response to the stimulation (Extended Data Fig. 2). Together, these data indicate that neuronal HMGB1 induces microglial activation and secretion of proinflammatory cytokines, C1q and type I IFN.

HMGB1 binds to numerous cell surface receptors, including RAGE[19]. As RAGE has been implicated in other disease models with neuroinflammation[18,23–25], we asked whether RAGE expression is necessary for microglial activation in our model of NPSLE (Fig. 2). We incubated microglia from RAGE-deficient (RAGE KO) mice with HMGB1 and found that the transcription of *Tnf*, *Il1b*, *C1qa* and *Ifnb1* was significantly attenuated in RAGE KO compared with WT microglia (Fig. 2a). We then asked whether microglial activation would occur in vivo in RAGE KO DNRAb$^+$ mice. DNRAbs are induced by peptide immunization only in H-2^d mice[26]. As we were unable to generate a C57BL/6 (B6) mouse with a recombination event that rendered it RAGE deficient on an H-2^d background, owing to the proximity of the genes encoding RAGE and major histocompatibility complex, we employed a model that we have used previously[5] and injected (B6) WT mice and (B6) RAGE KO mice with G11, a monoclonal DNRAb (mDNRAb$^+$), or B1, an isotype-matched monoclonal antibody with no detectable binding in the brain (mDNRAb$^-$)[27], followed by LPS administration. After 8 weeks, the CA1 region of the hippocampus was examined in each strain. Acute pyramidal neuron loss occurred in both RAGE KO mDNRAb$^+$ mice and WT mDNRAb$^+$ mice (Extended Data Fig. 3a). However, RAGE KO mDNRAb$^+$ mice developed neither microglial activation (Fig. 2b,c) nor decreased dendritic complexity, although this pathology was observed in WT mDNRAb$^+$ mice (Fig. 2d–f), demonstrating that RAGE expression is necessary for the development of the sustained neuropathology caused by DNRAbs.

ACE inhibitor effects are dependent on LAIR-1 expression

We have shown that, in the periphery, C1q can act as a modulating agent tempering the proinflammatory effects of HMGB1:RAGE signaling in monocytes[19,20,28]. Although complement frequently plays an anti-inflammatory role outside the brain, its function in the CNS is more complex and highly contextual[12,17,29,30]. C1q plays a pivotal role in synaptic pruning during development by tagging synapses for elimination[29]. Moreover, C1q appears to continue to play a role in synaptic remodeling throughout adulthood, and increasing evidence reveals that this process becomes maladaptive in the context of aging and brain injury[30,31]. For instance, Alzheimer's disease (AD) and other neurodegenerative diseases show increases in complement proteins in the brain and CSF[30]. Although C1q appears to contribute to a sustained inflammatory state in the CNS and is critical to the development of DNRAb-induced pathology, we reasoned that C1q might also mitigate microglial activation through binding the inhibitory receptor LAIR-1, as occurs in peripheral macrophages[20] because *Lair1* is expressed in microglia[32]. We further hypothesized that LAIR-1 might be reduced on hippocampal microglia of DNRAb$^+$ mice and increased after treatment with an ACE inhibitor. We therefore assessed the expression of *Lair1* in hippocampal microglia by reverse transcription quantitative PCR (RT–qPCR) and found that microglia isolated from DNRAb$^+$ mice indeed expressed significantly less *Lair1* transcript than microglia from

DNRAb$^-$ mice (Fig. 3a). We treated DNRAb$^+$ mice with the ACE inhibitor captopril, which penetrates the BBB, or enalapril, which does not[12]. We observed increased *Lair1* expression in hippocampal microglia isolated from captopril-treated mice compared with microglia from enalapril-treated mice, suggesting that LAIR-1 might indeed be an important regulator of the microglial activation state (Fig. 3b).

To confirm that the decrease in microglial activation and the increased neuronal dendrite arborization mediated by captopril are dependent on LAIR-1, we generated WT DNRAb$^+$ and DNRAb$^-$ mice and DNRAb$^+$ and DNRAb$^-$ mice with LAIR-1 deficiency in microglia (*Lyz2*-cre$^+$*Lair1*$^{fl/fl}$; termed LAIR-1 cKO). Although *Lyz2* is also expressed by peripheral monocytes and macrophages, we do not observe effects of peripheral myeloid cell activation or infiltration into the CNS in this model[5]. Both strains of DNRAb$^+$ mice developed acute neuronal loss in the hippocampal CA1 pyramidal layer (Extended Data Fig. 3b). Captopril treatment led to a lower activation score for microglia in DNRAb$^+$ WT mice; however, it did not affect the microglial activation state in DNRAb$^+$ LAIR-1 cKO mice (Fig. 3c,d). Moreover, captopril ameliorated the loss of dendritic complexity in DNRAb$^+$ WT mice but had no effect on dendritic arborization in DNRAb$^+$ LAIR-1 cKO mice (Fig. 3e,f). Together, these observations demonstrate that microglial LAIR-1 is essential for the regulation of inflammation and the neuroprotective effects of ACE inhibitors after DNRAb-mediated neuronal injury.

DNRAb$^+$ microglia show more reactive transcriptional profiles

To further interrogate the pathways activated by DNRAb in the hippocampus, we performed single-cell RNA sequencing (scRNA-seq) on hippocampal microglia from saline-treated DNRAb$^-$, saline-treated DNRAb$^+$ and captopril-treated DNRAb$^+$ mice. We identified six clusters of microglia by scRNA-seq (Fig. 4a and Extended Data Fig. 4), including two large clusters, one expressing genes characteristic of a healthy, quiescent homeostatic state (homeostatic) and one with high levels of the transmembrane chemosensor *Ms4a7* (Ms4a7$^+$)[33]. We also identified four very small clusters: one with *Top2a*$^+$ cycling cells (cycling), one with *S100a4*$^+$ microglia (S100a4$^+$), one with high expression of IFN-stimulated genes (IFN responsive)[33] and one with very low expression of *Tmem119* (Tmem119$^-$) which may be phagocytic microglia or macrophages[34–37].

We focused on the two larger clusters of microglia, the homeostatic and Ms4a7$^+$ clusters, because several mice provided <20 cells to each of the other clusters. Our analysis revealed significant differences in the proportion of each cluster between treatment groups in the homeostatic and Ms4a7$^+$ clusters, demonstrating that DNRAb$^+$ mice had an increased proportion of reactive microglia and that captopril treatment returns the proportions to control levels (Fig. 4b,c and Extended Data Tables 1–3), consistent with the data derived from immunohistology. Notably, the transcriptional profile of Ms4a7$^+$ microglia displays similarity to those of microglia with altered functionality from multiple models of CNS inflammation and neurodegeneration, including the disease-associated microglia (DAM)[35], NPSLE[38] and neurodegenerative microglia (MGnD)[39] gene signatures (Extended Data Fig. 5).

Comparison of differentially expressed genes (DEGs) among the experimental groups demonstrated that homeostatic microglia were qualitatively comparable in all groups, but Ms4a7$^+$ microglia were increased both in their relative frequency and in gene expression differences in DNRAb$^+$ mice (Fig. 4b–d and Extended Data Tables 2–5). Ms4a7$^+$ microglia from DNRAb$^+$ mice exhibited upregulation of genes associated with inflammation, phagocytosis and the DAM signature (*Cxcr4*, *Lgals3*, *Apoe*, *Ccl2*, *Lyz2*, *Tlr8* and *Nlrc5*) and downregulation of genes indicative of a more quiescent, basal state (*P2ry12*, *P2ry13*, *Sall1*, *Selplg*, *Olfml3*, *Siglech* and *Hexb*) compared with Ms4a7$^+$ microglia from DNRAb$^-$ and captopril-treated DNRAb$^+$ mice (Fig. 4d)[35]. In contrast, few genes were differentially expressed between DNRAb$^-$ mice and captopril-treated DNRAb$^+$ mice in the Ms4a7$^+$ cluster (Fig. 4d). Based on our in vitro data (Figs. 1–3), we analyzed Ms4a7$^+$ microglia from DNRAb$^+$ and DNRAb$^-$ mice for differential expression of inflammatory cytokines, type I IFN, complement and phagocytic pathways. Ms4a7$^+$ microglia from DNRAb$^+$ mice had increased expression of genes encoding the proinflammatory cytokines *Tnf* and *Il1b*, the type I IFN receptor *Ifnar1*, receptors for complement components such as *C3ar1* and *Cd93* and the phagocytosis-associated receptor tyrosine kinase *Axl* and lysosomal protein *Lyz2* compared with DNRAb$^-$ microglia (Fig. 4e and Extended Data Tables 4 and 5). These changes were either attenuated or abrogated completely in captopril-treated DNRAb$^+$ mice (Fig. 4e and Extended Data Tables 4 and 5).

ARB replicates effects of ACE inhibitors on neurons and microglia

ACE inhibitors affect both the renin–angiotensin and the kallikrein–kinin systems[40,41]. ACE converts ATI to ATII, which can induce a proinflammatory phenotype in microglia when it binds to AT1R[41]. ACE also degrades bradykinin, which exerts anti-inflammatory effects on microglia[42]. Moreover, bradykinin has been reported to decrease type I IFN production in bone marrow-derived dendritic cells[40,41] and captopril has been shown to decrease type I IFN production and improve behavioral symptoms in other mouse models of NPSLE[43].

We found that microglia stimulated with HMGB1 upregulated AT1R (*Agtr1a*) expression (Fig. 5a), suggesting that ATII signaling may be a mechanism by which captopril treatment is beneficial. We, therefore, treated mice with an ARB, telmisartan, which inhibits ATII signaling through AT1R, but does not affect the activity of ACE on bradykinin. We found that treatment with telmisartan phenocopied the effects of captopril on microglial activation as well as on neuronal dendritic complexity (Fig. 5b–e). Microglia from DNRAb$^+$ telmisartan-treated mice were significantly less activated than microglia from DNRAb$^+$ saline-treated mice and showed no significant differences in activation from microglia from DNRAb$^-$ mice treated with either telmisartan or saline (Fig. 5c). Correspondingly, telmisartan rescued the DNRAb$^+$-induced decrease in neuronal dendritic complexity. Dendritic arborization in DNRAb$^+$ telmisartan-treated mice was comparable to that of DNRAb$^-$ mice of either treatment group, abrogating the decrease seen in DNRAb$^+$ saline-treated mice (Fig. 5d,e). Together, these results demonstrate that ARB treatment can replicate the effects of ACE inhibition, thereby implicating decreased ATII/AT1R signaling in the protective mechanism of ACE inhibition.

HMGB1-induced IL-10 suppresses LAIR-1 expression

Our data demonstrate not only the activation of microglia through an ATII/AT1R pathway but also a need for *Lair1* in restoring microglial quiescence. As LAIR-1 has been shown to be modulated by the canonically anti-inflammatory cytokine IL-10 (ref. 44), we looked at *Il10* gene expression in our scRNA-seq analysis. Somewhat surprisingly, DNRAb$^+$ Ms4a7$^+$ microglia expressed significantly higher levels of *Il10* than DNRAb$^-$ microglia. Captopril-treated DNRAb$^+$ microglia showed lower levels of expression compared with untreated DNRAb$^+$ microglia, although this decrease did not reach statistical significance (Fig. 6a). We looked to see whether this difference in expression was mediated by HMGB1 levels. We found that ex vivo isolated microglia stimulated with HMGB1 indeed significantly upregulated *Il10* expression compared with unstimulated controls (Fig. 6b). We then cultured microglia with IL-10 to determine whether this, in turn, affected *Lair1* expression. Ex vivo isolated microglia cultured with 20 ng ml^{-1} of IL-10 exhibited significantly lower levels of *Lair1* expression compared with unstimulated microglia (Fig. 6c). Thus, IL-10 can be induced by HMGB1 and suppresses *Lair1*.

Discussion

We have demonstrated that, after a self-limited, antibody-mediated insult, the CNS can enter a sustained neuroinflammatory state. Secretion of HMGB1 by DNRAb-damaged neurons activates microglia and causes them to secrete proinflammatory cytokines, C1q and type I IFN, a process that depends on RAGE expression in microglia. HMGB1 not only acts as a DAMP to activate microglia but also binds the NMDAR on neurons and can potentiate NMDAR signaling[13]. IL-1β, which microglia secrete in response to HMGB1, can bind the neuron-specific IL-1R accessory protein AcPb, which potentiates calcium influx after IL-1β and NMDAR signaling[45]. Increased NMDAR signaling strength leads to greater synaptic activity in the remaining neurons, which is consistent with our observations of brain metabolic changes in DNRAb$^+$ mice using [^{18}F]fluorodeoxyglucose positron emission tomography imaging[46]. Increased NMDAR signaling leads to more secretion of HMGB1, initiating a self-reinforcing cycle, with HMGB1 potentiating NMDAR signaling itself as well as indirectly through stimulating microglial IL-1β secretion[1,13,45]. The secreted C1q binds HMGB1, thereby decorating HMGB1-bound NMDARs[1], likely acting as an opsonin on neuronal synapses to induce aberrant dendritic pruning and, ultimately, a loss of dendritic arborization and impaired spatial memory[1]. HMGB1 induces microglia to produce IL-10, which decreases *Lair1* expression, ensuring that C1q engages scavenger receptors rather than engaging the inhibitory LAIR-1. Treatment with an ACE inhibitor or ARB decreases ATII/AT1R signaling in microglia, which creates a less inflammatory environment that will result in less HMGB1 secretion. Diminishing HMGB1 decreases both IL-10 secretion and its suppression of *Lair1*. Sufficient *Lair1* expression allows microglia to re-establish a healthy, quiescent state and break the inflammatory cycle (Fig. 7).

The precipitating event of DNRAb penetration into the brain and the neuronal death this causes are transient, but the ensuing state of microglial activation and loss of dendritic complexity is sustained, which may explain the persistent cognitive dysfunction seen in patients with SLE. The inflammatory environment and loss of synapses through a

complement-dependent microglial process creates a self-perpetuating state of increased synaptic activity and HMGB1 secretion. HMGB1 has also been shown to induce neurite retraction and degeneration directly through TLR4, which also functions as a receptor for HMGB1 (ref. 47).

The molecules and mechanisms that we have delineated in this model appear to be common mechanisms of neuroinflammation in many contexts. Chronic neuroinflammation is associated with many conditions of cognitive dysfunction and many neurodegenerative diseases. It is increasingly understood to be an underlying causative factor of pathology in AD and other forms of dementia, amyotrophic lateral sclerosis, multiple sclerosis, post-sepsis and postoperative cognitive dysfunction, and traumatic brain injuries, in addition to NPSLE[23,48]. HMGB1, RAGE, TNF, IL-1β and C1q have all been specifically implicated; HMGB1 has been identified as a risk factor for memory impairment, chronic neurodegeneration and progression of neuroinflammation in AD, Parkinson's disease (PD), multiple sclerosis and sepsis-surviving mice[49–51], and increased levels of HMGB1 after an injury to the brain correlate with neuronal degeneration, dependent on microglial activation[24]. In fact, hippocampal neurons cultured with amyloid-β increased expression of HMGB1, RAGE, TLR4, IL-1β, IL-6 and TNF, directly implicating the same mechanistic pathway as we identified here in AD pathogenesis[23], although the trigger in AD is an ongoing CNS abnormality. Moreover, in models of postoperative and post-sepsis cognitive dysfunction, treatment with an anti-HMGB1 antibody prevented memory deficits[25,49], providing direct evidence for the importance of HMGB1. Importantly, RAGE expression in the hippocampus and cortex in AD brains has also been shown to correlate with brain pathology[23].

Complement and C1q are specifically known to mediate aberrant microglial synaptic pruning in AD and other neurodegenerative diseases[52–54]. Indeed, increased complement activation and deposition have been found in postmortem tissue from patients with AD and PD, and studies in animal models have shown a similar increase in complement components, synaptic loss and cognitive dysfunction, even before widespread protein aggregation occurs[54]. We have demonstrated in our model that HMGB1 not only binds synaptic proteins but also increases the amount of C1q localized to synapses by acting as a bridge, indicating that this is the probable mechanism by which the decreased dendritic arborization occurs[12], although there are nonphagocytic, microglia-dependent mechanisms by which synapse elimination can occur as well[55]. As increasing activation of the NMDAR causes neuronal secretion of HMGB1 in an NMDAR-ligand concentration-dependent manner[12,56], a self-perpetuating cycle involving inflammation, synapse elimination and resulting cognitive dysfunction is established.

We were able to disrupt this pernicious cycle using ACE inhibition or AT receptor blockade, both of which function to decrease the activation of AT1R. ATII signaling through AT1R induces a proinflammatory phenotype in microglia with increased proinflammatory and reactive oxygen species (ROS), which can damage neurons[41,57,58]. In neurons, ATII signaling through AT1R induces increased calcium influx, ROS and oxidative stress[59,60]. The proinflammatory effects of the renin–angiotensin system have been implicated in the pathogenesis and associated cognitive dysfunction of AD, PD and vascular and ischemic

dementia[41,57], and centrally acting ACE inhibitors and ARBs have been successfully used to improve cognitive function in AD[41,60–63]. We have shown that microglial *Lair1* expression is required for ACE inhibition to be effective. Microglial *Lair1* is suppressed by IL-10, which is induced by HMGB1. Increased levels of IL-10 have been shown in the CSF of patients with NPSLE and high IL-10 levels in the CSF have been identified as part of a panel of six cytokines that predicted a lack of responsiveness to treatment on neuropsychiatric symptoms (treatment included glucocorticoid treatment and the addition of induction therapies for some patients)[64]. How IL-10 suppresses *Lair1* expression is not known. Of note, LAIR-1 can also bind collagen. We were unable to test directly whether it was uniquely an interaction of LAIR-1 with C1q that led to a restoration of a healthy homeostasis because C1q is necessary for pathology in our model to occur[12].

The transcriptomic analysis of hippocampal microglia shows them to be largely separated into two distinct clusters in this model: the homeostatic cluster expresses genes characteristic of quiescent homeostatic state and the Ms4a7^{+} cluster expresses genes associated with a more reactive microglial phenotype that resembles microglial gene signatures described in other neuroinflammatory contexts, including DAM[35], NPSLE[38] and MGnD[39] microglia. Although the homeostatic microglia are proportionately decreased in DNRAb^{+} mice, they appear to be qualitatively similar in all groups. Microglia from the Ms4a7^{+} cluster are not only proportionately increased in DNRAb^{+} mice, but also transcriptionally distinct from DNRAb^{-} and captopril-treated DNRAb^{+} Ms4a7^{+} microglia, and reflect a more reactive and inflammatory state that is consistent with the phenotype that was observed in this model. It is notable that the Ms4a7^{+} cluster exhibits similarities in expression to one identified by Hammond et al.[33], which was found to have the highest expression in e14.5 embryos but exhibited substantial similarity to microglia surrounding demyelinated lesions[33]. The authors of this study also note the commonalities of this cluster with the DAM transcriptomic signature[33]. Many other studies have observed that microglia in an inflammatory, injury or neurodegenerative context re-express developmental markers as well[33]. Our observation that microglia cultured from neonatal mice have similar but outsized responses to inflammatory stimuli compared with adult microglia ex vivo is consistent with this observation.

Thus, neuronal stress, HMGB1 secretion, microglial activation with low expression of *Lair1* and C1q-dependent loss of dendrites defines a new, albeit maladaptive, equilibrium. We posit that a healthy equilibrium is restored when C1q pivots and binds to LAIR-1 rather than scavenger receptors to suppress microglial activation. This model informs our understanding of NPSLE. Subjects with cognitive dysfunction exhibit specific alterations in the hippocampus, such as hypermetabolism indicative of increased synaptic activity, which would lead to increased secretion of HMGB1, microglial activation and BBB impairment, all of which are reproduced faithfully in the murine model[2–4,10–12,46,65]; the data presented in the present study show that CNS inflammation may continue long after the triggering insult and that patients with quiescent systemic disease may still exhibit such inflammation. Increasing LAIR-1 expression using ACE inhibition or AT receptor blockade may be of therapeutic benefit in NPSLE, and likely in other conditions with ongoing sustained neuroinflammation, some of which are already known to respond to ACE inhibition[66].

The present study shows how inflammation can be sustained in a feedforward process despite no intrinsic, genetically determined abnormality of neurons or microglia and no continuing external triggers for inflammation. Although there have been studies that describe ongoing neuronal–glial interactions that maintain CNS health[67], there are no similar studies to explain the ongoing interactions that sustain inflammation. Thus, our data represent a major advance in our understanding of neuroinflammation with the translational implication that there needs to be a direct manipulation of the cells in the CNS to modulate or abort the inflammatory process.

Online content

Any methods, additional references, Nature Portfolio reporting summaries, source data, extended data, supplementary information, acknowledgements, peer review information; details of author contributions and competing interests; and statements of data and code availability are available at https://doi.org/10.1038/s41590-024-01772-6.

Methods

Mice

Mice were housed in the Center for Comparative Physiology at the Feinstein Institutes for Medical Research on a 12-h light cycle at 70 °C with 30% humidity. Mice were freely fed Irradiated PicoLab Rodent Diet 20 chow (LabDiet, catalog no. 5053). C57BL/6 (B6), B6.C-H2d/bByJ (B6.H2^{d}) and BALB/cJ (Balb/c) mice were purchased from the Jackson Laboratory. B6 RAGE KO mice were a generous gift from K. Tracey of the Feinstein Institutes for Medical Research. LAIR-1 cKO mice were generated by crossing B6.129P2-Lyz2$^{tm1(cre)}$Ifo/J with B6.Cg-Lair1^{tm1Jco}/J (Jackson Laboratory) after backcrossing on to the B6.H2^{d} background. B6.Cg-Tg(Camk2a-cre)T29–1Stl/J and Hmgb1$^{tm1.1Rshw}$/J mice (Jackson Laboratory) were crossed with in-house B6.H2^{d} mice to generate Camk2a-cre HMGB1$^{fl/fl}$ B6.H2^{d} mice. All adult mice used were female. All procedures using mice were conducted using protocols approved by the Feinstein Institutes of Medical Research Institutional Animal Care and Use Committee (protocol nos. 2009–048 and 2022–023).

Treatment

Female mice were immunized as previously described[4,12]. Briefly, mice were injected intraperitoneally (i.p.) beginning at age 6–8 weeks with DWEYS peptide multimerized on a poly(lysine) backbone (termed DNRAb^{+}; AnaSpec, catalog no. AEJR-1) or with the poly(lysine) backbone alone (termed DNRAb^{-}; AnaSpec, catalog no. AS-21006) emulsified with an equal volume of complete Freund's adjuvant (BD Biosciences, catalog no. 263810) and boosted with two incomplete Freund's adjuvant (BD Biosciences, catalog no. 263910) emulsions spaced 2 weeks apart (1 mg ml^{-1} of final peptide concentration). Two weeks after the last immunization, mice were injected i.p. with 5 mg per kg body weight of LPS (Sigma-Aldrich, catalog no. L4524, lot no. 107M4048V) 48 h apart. B6 and RAGE KO mice were passively immunized with 400 μg of intravenously injected monoclonal antibody G11 (mDNRAb^{+}) or B1 (mDNRAb^{-}), produced in house as described previously[27]. Mice treated with an ACE inhibitor, captopril (Sigma-Aldrich, catalog no. C8856) or enalapril

(USP, catalog no. 1235300), received once-daily i.p. injections at 5 mg per kg body weight for 2 weeks, beginning 5 weeks after the second LPS injection. Control mice received an equivalent volume of sterile saline based on body weight. The ARB telmisartan (Sigma-Aldrich, catalog no. T8949) was administered freely at ~1 mg per kg body weight in water for 2 d beginning 1 week after the second LPS injection.

Isolation of microglia

Mice were anesthetized with Euthasol (Virbac) and perfused with pre-perfusion buffer containing 0.5% sodium nitrite, 0.9% sodium chloride and 0.1% heparin. The brain was extracted and tissue was manually dissociated on ice, followed by enzymatic dissociation using the Neural Tissue Dissociation Kit (Miltenyi Biotec) according to the manufacturer's instructions. Microglia were then isolated using Myelin Removal Beads II (Miltenyi Biotec) or Debris Removal Solution (Miltenyi Biotec)[68]. Microglia used for RT–qPCR analysis were further sorted using CD11b MicroBeads (Miltenyi Biotec) and lysed for RNA extraction immediately or after culturing, as described. Microglia used for scRNA-seq analysis were FACS sorted using Live/Dead Fixable Violet (1:500, Life Technologies, catalog no. L34964), FITC rat anti-mouse CD45 (1:100, BD Biosciences, clone 30-F11) and PE rat anti-mouse CD11b (1:100, BD Biosciences, clone M1/70).

Primary microglia culture preparation

Primary microglia were isolated from P0–3 C57BL/6 or RAGE KO pups using the shaking method, adapted from previously described protocols[22]. Briefly, P0 litters were euthanized via decapitation and the brains were removed and collected under aseptic conditions. Brain tissue was dissociated to a single-cell suspension using the Neural Tissue Dissociation Kit and the resulting cell suspension was centrifuged at 400*g* for 10 min. The cells were then resuspended in complete Dulbecco's modified Eagle's medium (with 4.5 g l^{-1} of glucose) containing 10% fetal bovine serum, 1% penicillin–streptomycin and 0.5 ng ml^{-1} of recombinant mouse granulocyte–macrophage colony-stimulating factor (R&D Biosystems) before being filtered through a 70-μm cell strainer (Corning, catalog no. 431751). Cell suspensions from each litter of pups were plated into a different 175-cm^2 flask and cultured until confluence (7–10 d). Microglia were recovered from culture by manual shaking. Growth medium containing 'shaken' microglia was centrifuged at 400*g* for 10 min, then counted and plated alone in a 48-well plate at 200,000 cells per well. Flow cytometry analysis using antibodies against CD45 (1:80, BioLegend, clone 30-F11), CD11b (1:200, BD Biosciences, clone M1–70) and transmembrane protein 119 (Tmem119; 1:500, Abcam, clone 106–6) indicated a microglial purity of >95%.

Cell culture treatment

Primary microglia were allowed to attach overnight in serum-free X-VIVO medium (Lonza Bioscience) before being treated with HMGB1 (100, 500 or 1,000 ng ml^{-1}) or IFN-β (1,000 or 100,000 units). Cells were left to incubate in treatments for 4.5 h for analysis of lysate by RT–qPCR, and 24 h for analysis of cell culture supernatant by ELISA. Adult ex vivo microglia were isolated as described above and cultured in X-VIVO medium with HMGB1 (1,000 ng ml^{-1}) or IL-10 (20 ng ml^{-1}) for 6 h. HMGB1 was obtained as a generous gift from K. Tracey of the Feinstein Institutes for Medical Research. IFN-β was purchased from R&D

Biosystems (catalog no. 8234-MB-010/CF). IL-10 was purchased from R&D Biosystems (catalog no. 217-IL-010).

RNA isolation, cDNA synthesis and RT–qPCR

Total RNA was extracted from microglia using the QIAGEN RNeasy RNA extraction kit according to the manufacturer's instructions. Briefly, cells from each well were homogenized in RLT lysis buffer. The homogenate was then passed through QIAshredder spin columns to remove cellular debris and RNA was purified using RNeasy spin columns. RNA was eluted in 60 µl of RNase-free H_2O and the quality and quantity of RNA were measured using NanoDrop. Reverse transcription of RNA was performed using the iScript Reverse Transcription Mix (BioRad) according to the manufacturer's protocol. Briefly, 15 µl of RNA was mixed with a reaction mixture including iScript Reverse Transcriptase enzyme and the reaction was incubated at the recommended temperature cycle for complementary DNA synthesis. RT–qPCR was performed using TaqMan Gene Expression Assays (Thermo Fisher Scientific) on a Roche LightCycler 480. TaqMan PreAmp Master Mix was used for adult ex vivo RT–qPCR experiments (TaqMan, catalog no. 4384266). Reactions were performed according to the manufacturer's instructions. Gene expression levels were normalized to the expression of *Polr2a* using the ΔC^t method. Relative expression levels were calculated using the $\Delta\Delta C^t$ method. Primers used for RT–qPCR include: *Polr2a* (Mm00839493_m1, TaqMan); *Tnf* (Mm00443298_m1, TaqMan); *Il1b* (Mm00434228_m1, TaqMan); *C1qa* (Mm07295529_m1, TaqMan); *Ifnb1* (Mm00439552_s1, TaqMan); *Lair1* (Mm00618113_m1, TaqMan); *Agtr1a* (Mm0195772_s1, TaqMan); and *Il10* (Mm01288386_m1, TaqMan).

ELISA

Cell culture supernatant was collected from 24-h treated microglia and spun down at 500*g* for 5 min followed by separation of supernatant. The Duoset TNF-α, Duoset IL-1β and Duoset IFN-β ELISAs (R&D Biosystems) were performed on supernatant according to the manufacturer's instructions. Briefly, 96-well microplates were coated with the appropriate capture antibody and incubated overnight at 4 °C. Plates were washed and blocked with 1% bovine serum albumin (BSA) for 1 h. Samples and standards were added to the wells and incubated for 2 h. After washing, detection antibody was added and incubated for 2 h. Streptavidin–horseradish peroxidase conjugate was added and incubated for 20 min. The wells were washed and substrate solution was added for a 30-min incubation. Stop solution was added to terminate the reaction and the absorbance was read at optical density at 450 nm using a microplate reader. Data were analyzed using a standard curve generated from the known standards provided in the kit and statistical analysis was performed using GraphPad Prism.

Immunohistochemistry

Mice were anesthetized with Euthasol or isoflurane (1.5%; Henry Schein Animal Health, catalog no. NDC11695-6776-2) and perfused with pre-perfusion buffer containing 0.5% sodium nitrite, 0.9% sodium chloride and 0.1% heparin, which was followed by 4% paraformaldehyde (PFA) in 0.1 M phosphate buffer. Brains were post-fixed in 4% PFA for 6–24 h, followed by 30% sucrose for 1–3 d, and sliced into 40-µm sections. Tissue was

permeabilized using 0.2% Triton X-100 in 1% BSA in phosphate-buffered saline (PBS) and blocked with 1% BSA in PBS for 1 h. Primary antibody staining was performed overnight at 4 °C using rabbit anti-mouse Iba-1 (1:500; Wako Chemical, catalog no. 019–19741) and CD68 (1:200; BioRad, catalog no. MCA1957) with secondary staining performed for 45 min at room temperature using Alexa Fluor-594 donkey anti-rabbit (1:400; Invitrogen, catalog nos. A32754 and A21207), goat anti-rabbit (1:400; Invitrogen, catalog no. A11037), donkey anti-rat (1:400; Invitrogen, catalog no. A21209), Alexa Fluor-488 goat anti-rat (1:400; Invitrogen, catalog no. A11006), donkey anti-rabbit (1:400; Invitrogen, catalog no. A21206) or donkey anti-rat (1:400; Invitrogen, catalog no. A21208), and Alexa Fluor-647 goat anti-rat (1:400; Invitrogen, catalog no. A21247) and mounted with DAPI Fluoromount-G medium (Southern Biotech, catalog no. 0100–20). Neuronal 3,3′-diaminobenzidine (DAB) staining used to quantify acute neuronal loss was performed using anti-NeuN (1:200; EMD Millipore, catalog no. MAB377) with secondary antibody biotin horse anti-mouse IgG (1:200; Vector Labs, catalog no. BA-2000). Sections were washed (0.1 M PBS and 0.1 M phosphate buffer (PB)) and incubated with Vectastain Elite ABC-HRP Kit (1:200; Vector Laboratories, catalog no. PK-6100). Sections were developed for 5 min in DAB solution (5 mg ml^{-1} of DAB, 0.1 M PB, 0.000036% H_2O_2; Sigma-Aldrich, catalog no. D-5637). Acute neuronal loss in the CA1 region of the hippocampus was quantified as described previously[4]. Neuronal Golgi staining used to visualize neurons for Sholl dendrite analyses was performed using FD Rapid Golgi Stain kit (FD NeuroTechnologies), as previously described[10]. Briefly, brains were extracted and immersed in impregnation solution for 2 weeks, sectioned at 100 μm and stained with silver nitrate solution for 10 min.

Microscopy

The tissues used for immunohistochemistry were imaged using Zeiss LSM 880 confocal microscope (Airyscan, 0.8 numerical aperture) and processed using Zen Black software (v.2.3 Sp1) and Zen Blue software (v.2.6). Microglial activation was scored as previously described[12,17,21], in which microglial morphology was scored: 0, <6 thin processes; 0.5, >6 but <12 thin processes; 1, 5–15 thick processes with branches; 2, 1–5 thick processes without branches; or 3, no clear processes. Microglial CD68 was scored: 0, little or no expression; 1, punctate expression; or 2, aggregate or punctate expression all over the cell. Composite activation scores were generated using the sum of both scores for each microglia. Tissues used for neuron quantification and Sholl analyses were imaged using an AxioImager ZI (Zeiss, ×100 oil, $z = 0.2–0.46$ μm for neuron quantification; ×40, $z = 2.0$ μm for dendrite measurement; ×100, $z = 0.5$ μm for spine density) using Zen Blue software (v.3.1) and were processed using Zen Blue software (v.2.6 and v.3.1). Image stacks for neuronal quantification were analyzed using StereoInvestigator programs in Neurolucida360 (MBF Bioscience). Images for Sholl analyses were analyzed on Neurolucida360. All raw measurements were compiled for cumulative probability distributions and analyzed by linear mixed model statistics. Dendrite lengths were collected within radii shells in the neurons of mice. The dendrite length within each radial shell per neuron per mouse was the unit of observation. Radial shells were nested within neurons, which were nested within mice. A three-level linear mixed model was performed to determine whether treatment and condition were associated with dendrite length. Random intercepts for mouse and neuron were included to account for the correlation with these clusters. An interaction between treatment

and condition was included to evaluate potential differential effects owing to treatment and condition groups. If significant ($P < 0.05$), pairwise comparisons were evaluated and Bonferroni's correction was applied to correct for multiple testing. If the interaction was not significant, the model was performed again, including treatment and condition as the main effects. The estimated mean dendrite length by treatment and condition and corresponding 95% confidence intervals were reported. The intraclass correlation coefficient, a measure of the proportion of variation explained by neuron and mouse cluster, was also reported. The nlme package was used to perform the mixed model within the R program v.3.6.1 with R studio.

ScRNA-seq

Hippocampal microglia were extracted and isolated from mice as described above. Library preparation was performed according to the manufacturer's instructions (Next GEM Single Cell 3′GEM v.3.1 protocol, 10x Genomics). Briefly, microglia were resuspended in the master mix and loaded together with partitioning oil and gel beads into the chip to generate the gel bead-in-emulsion (GEM). The RNA from the cell lysate contained in every single GEM was retrotranscribed to cDNA, which contains an Illumina R1 primer sequence, unique molecular identifier (UMI) and a 10× bead barcode. The pooled barcoded cDNA was then cleaned up with Silane DynaBeads, amplified by PCR and the appropriately sized fragments were selected with SPRIselect reagent for subsequent library construction. During the library construction, Illumina R2 primer sequence, paired-end constructs with P5 and P7 sequences and a sample index were added. Samples were sequenced by Genewiz (Azenta Life Sciences), 2 × 150 bases on an Illumina HiSeq X10. FASTQ data from 10× Chromium were processed with CellRanger v.6.1.2 (ref. 69), aligning to the C57BL/6 reference genome. The resulting count matrices were down-sampled using the downsampleReads function in DropletUtils v.1.14.2 (ref. 70), so that each mouse had the same number of reads per cell on average (based on the number of reads per cell returned by CellRanger). Empty droplets were identified with the emptyDropsCellRanger function in DropletUtils, setting the number of expected cells set to match the number estimated by CellRanger and otherwise using default parameters. The resulting matrices were combined into one joint matrix. This matrix was loaded into Seurat v.4.0.0 (ref. 71) with min.features = 300. The data were normalized to log(counts per million) and the data were scaled, regressing out the number of genes per cell (nFeature_RNA column in the metadata). Principal component analysis was calculated with RunPCA, followed by a uniform manifold approximation and projection (UMAP) being calculated with RunUMAP and dims = 1:15 and otherwise default parameters. The data were clustered with the FindNeighbors and FindClusters functions with dims.use = 1:15, and otherwise default parameters. Doublet scores were calculated with scds v.1.6.0 (ref. 72). Cell types were identified using known transcriptional markers (including *Snap25* for neurons, *Pdgfra* for oligodendrocyte precursor cells, *Plp1*/*Mobp* for oligodendrocytes, *Csf1r* for microglia, *Flt1* for endothelial cells, *Slc1a3*/*Gfap*/*S100b* for astrocytes, *Gad1*/*Gad2* for inhibitory neurons and *Slc17a6*/*Slc17a7* for excitatory neurons) and using Azimuth v.0.3.2 (ref. 71) with data from the Allen Brain Atlas used as a reference (downloaded from https://portal.brain-map.org/atlases-and-data/rnaseq/mouse-whole-cortex-and-hippocampus-10x). Clusters consisting of nonmicroglia cell types and doublets were removed. This resulted in 18,569 microglia split over 3 mice per condition, with 2,515

Ms4a7^{+} microglia and 15,285 homeostatic microglia. Previously published datasets were used in identifying and naming microglial clusters[33,73]. Cell-type composition analysis was performed with the propeller.anova function in the speckle v.0.0.2 package[74], using the asin normalization and otherwise default parameters and performing Benjamini–Hochberg multiple hypothesis correction. This was followed by post-hoc pairwise analyses with propeller.ttest (two-sided test based on a moderated Student's *t*-test) and Holm–Šídák multiple hypothesis correction. Differential expression between conditions was performed using a pseudobulk-based procedure[75], by summing up the per gene UMI counts for all cells in each sample and fitting a model with EdgeR v.3.32.1 (ref. 76) using the likelihood ratio test (assumes a negative binomial model), followed by correcting *P* values with fdrtool v.1.2.16 (ref.77) and performing Benjamini–Hochberg multiple hypothesis correction, and the results were reported for each comparison of interest. Enrichment analysis was performed using fgsea v.1.16.0 (ref. 78) and gene set scoring was performed with the AddModuleScores function in Seurat. Differential expression between clusters was performed using presto v.1 (ref. 79) (Wilcoxon's rank-sum test, two sided). The DAM and homeostatic gene sets were extracted from Table S2 in Keren-Shaul et al.[35], the NPSLE gene set was extracted from Fig. 5 in Makinde et al.[38] and the MGnD gene set was extracted from the 'Common affected genes' tab in Table S1 from Krasemann et al.[39].

Statistical analyses

GraphPad Prism (v.10, GraphPad Software) was used for all statistical comparisons unless otherwise noted. Analysis of variance (ANOVA), Student's *t*-test, Mann–Whitney *U*-test and Kruskal–Wallis test were performed as indicated. R (v.4.2.2) was used to perform linear mixed model analyses for Sholl analyses. $P < 0.05$ was considered statistically significant. No statistical methods were used to predetermine sample sizes but sample sizes were similar to those reported in previous publications[12]. Data distribution was assumed to be normal but this was not formally tested. Experimental conditions including immunization and treatment groups were assigned randomly. Data collection and analysis for RT–qPCR, ELISA and scRNA-seq were not performed blind to the conditions of the experiments. Data collection and analysis for all imaging and histology, including microglial activation scoring, tracing for Sholl analyses and spine density, and neuronal counts were performed blind to the conditions of the experiments. No animals or data points were excluded from the analyses, although mice with insufficient antibody titers were not used for experiments and tissue samples and images judged to be of insufficient quality were not used for data collection.

Extended Data

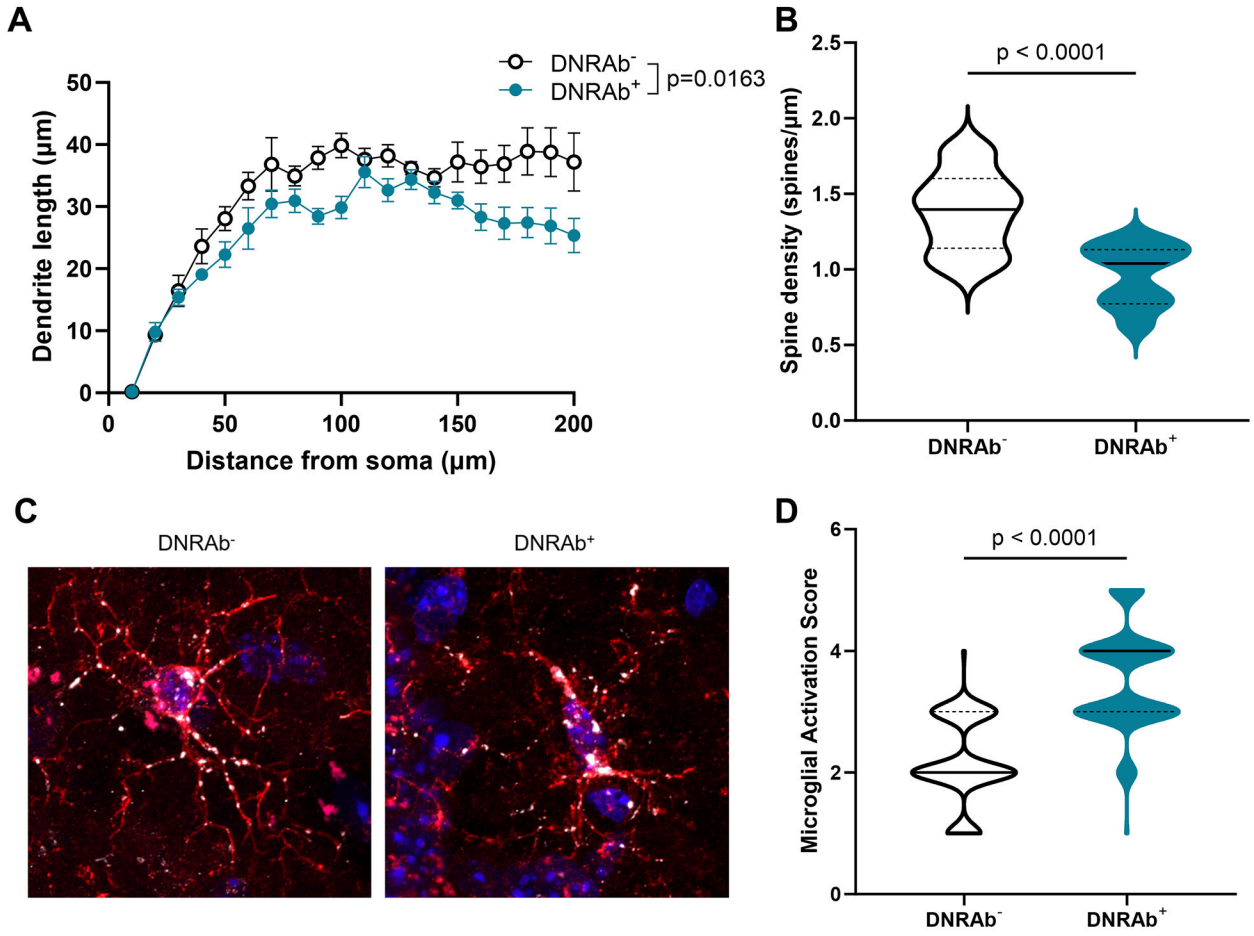

Extended Data Fig. 1 |. Pathology is sustained for at least 12 months.

a) Decreased dendritic complexity in 12 month old (m.o.) Balb/c DNRAb^{+} compared with DNRAb^{-} mice (mean +/− SEM; n = 4–5 mice per group; n = 55–59 neurons analyzed per group; two-tailed linear mixed model test with Tukey adjustment; p = 0.016). **b)** Decreased dendritic spine density in 12 m.o. Balb/c DNRAb^{+} compared with DNRAb^{-} mice (median (solid line) with quartiles (dash); n = 4 mice per group; n = 15–18 neurons analyzed per group; two-tailed Mann-Whitney test; p < 0.0001). **c)** Representative sections of microglia in CA1 stratum radiatum stained for Iba1 (red) and CD68 (white) in 12 m.o. DNRAb^{+} and DNRAb^{-} Balb/c mice (n = 3 mice per group). **d)** Increased activation score in 12 m.o. Balb/c DNRAb^{+} microglia compared to 12 m.o. Balb/c DNRAb^{-} counterparts based on morphology and CD68 expression (median (solid line) with quartiles (dash); n = 3 mice per group; n = 110–169 microglia scored per group; two-tailed Mann-Whitney test; p < 0.0001).

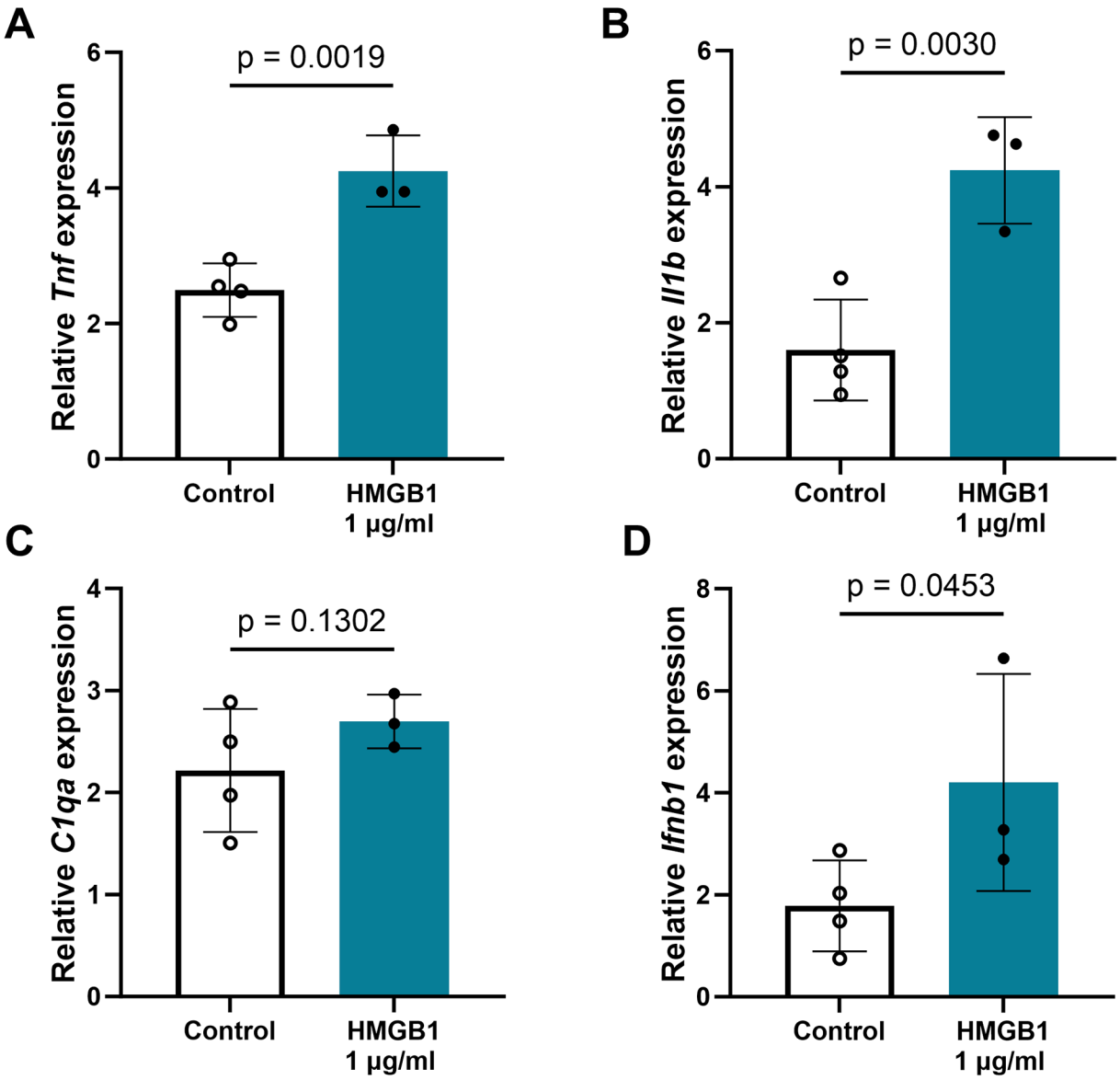

Extended Data Fig. 2 |. Ex vivo adult microglia and neonatal cultures respond similarly to HMGB1.

Increased mRNA expression for **a)** *Tnf* (p = 0.0019); **b)** *Il1b* (p = 0.0030); **c)** *C1qa* (p = 0.1302); and **d)** *Ifnb1* (p = 0.0453) in B6 microglia stimulated with 1 µg/ml HMGB1 compared with unstimulated microglia cultured in medium for 6 hours (mean +/− SD; *ex vivo* microglia isolated from 3–4 B6 mice; two-tailed unpaired t-test).

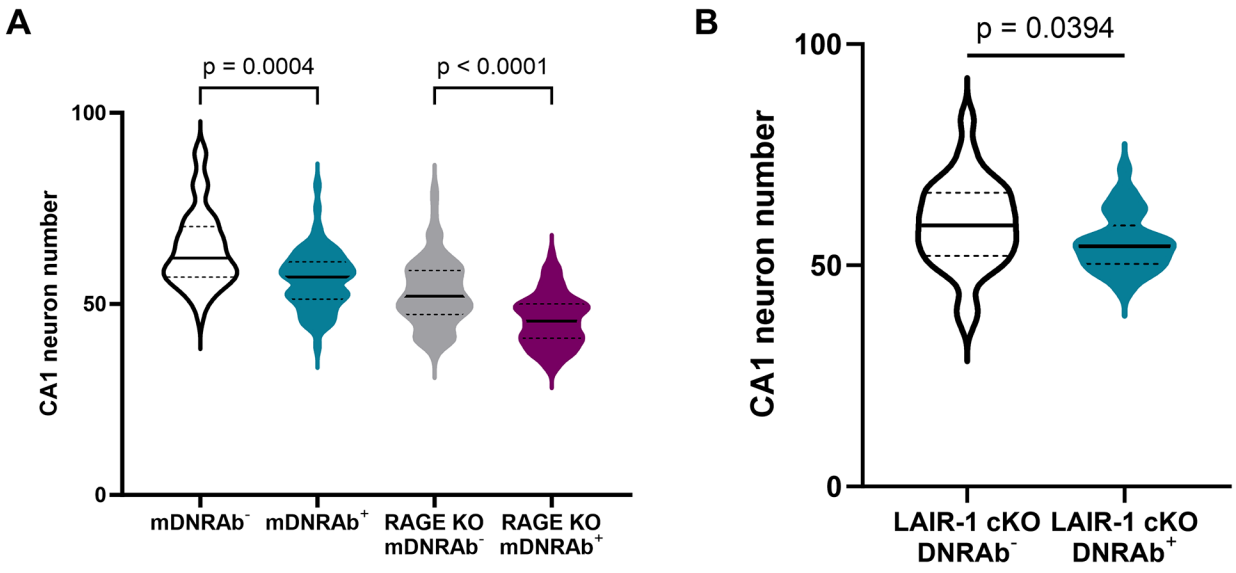

Extended Data Fig. 3 |. Acute neuronal loss is not affected by loss of RAGE or microglial LAIR-1.

a) Decreased CA1 neurons in WT B6 ($p = 0.0004$) and RAGE KO mDNRAb$^+$ ($p < 0.0001$) mice compared to their mDNRAb$^-$ counterparts (median (solid line) with quartiles (dash); n = 3–4 mice per group; n = 72–96 sections per group; two-tailed Kruskal-Wallis test). **b)** Decreased CA1 neurons in LAIR-1 cKO DNRAb$^+$ mice compared to DNRAb$^-$ (median (solid line) with quartiles (dash); n = 3 mice per group; n = 67–98 sections per group; two-tailed Mann-Whitney test; $p = 0.0394$).

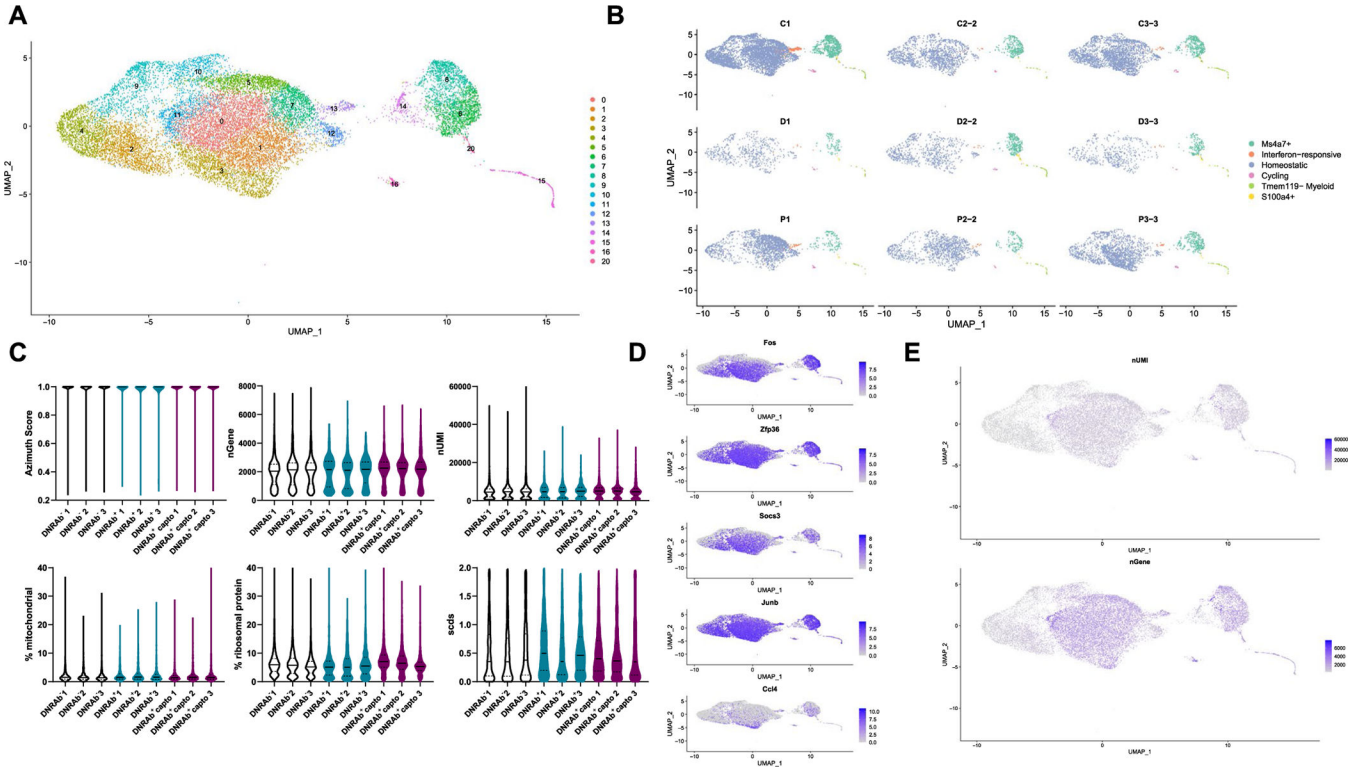

Extended Data Fig. 4 |. Single-cell RNA-seq clustering and quality control.

a) UMAP plot colored by clustering. **b)** UMAP plot split by mouse of origin, colored by cell type. No evidence of strong batch effects in the UMAP space. **c)** Violin plot of various QC metrics of interest, with similar distributions observed in each mouse. QC metrics include the score returned by Azimuth (Azimuth Score), number of genes per cell (nGene), number of UMI per cell (nUMI), percent UMI coming from mitochondrial reads (Percent Mitochondrial), percent UMI mapping to ribosomal proteins (Percent Ribosomal Protein), and doublet scores (scds). **d)** Feature plots of genes associated with a known microglia activation signature[73]. Subclustering within microglia subtypes is largely driven by these variables. **e)** Feature plots of number of genes per cell (nGene) and number of UMIs per cell (nUMI). Subclustering within microglia subtypes is largely driven by these variables.

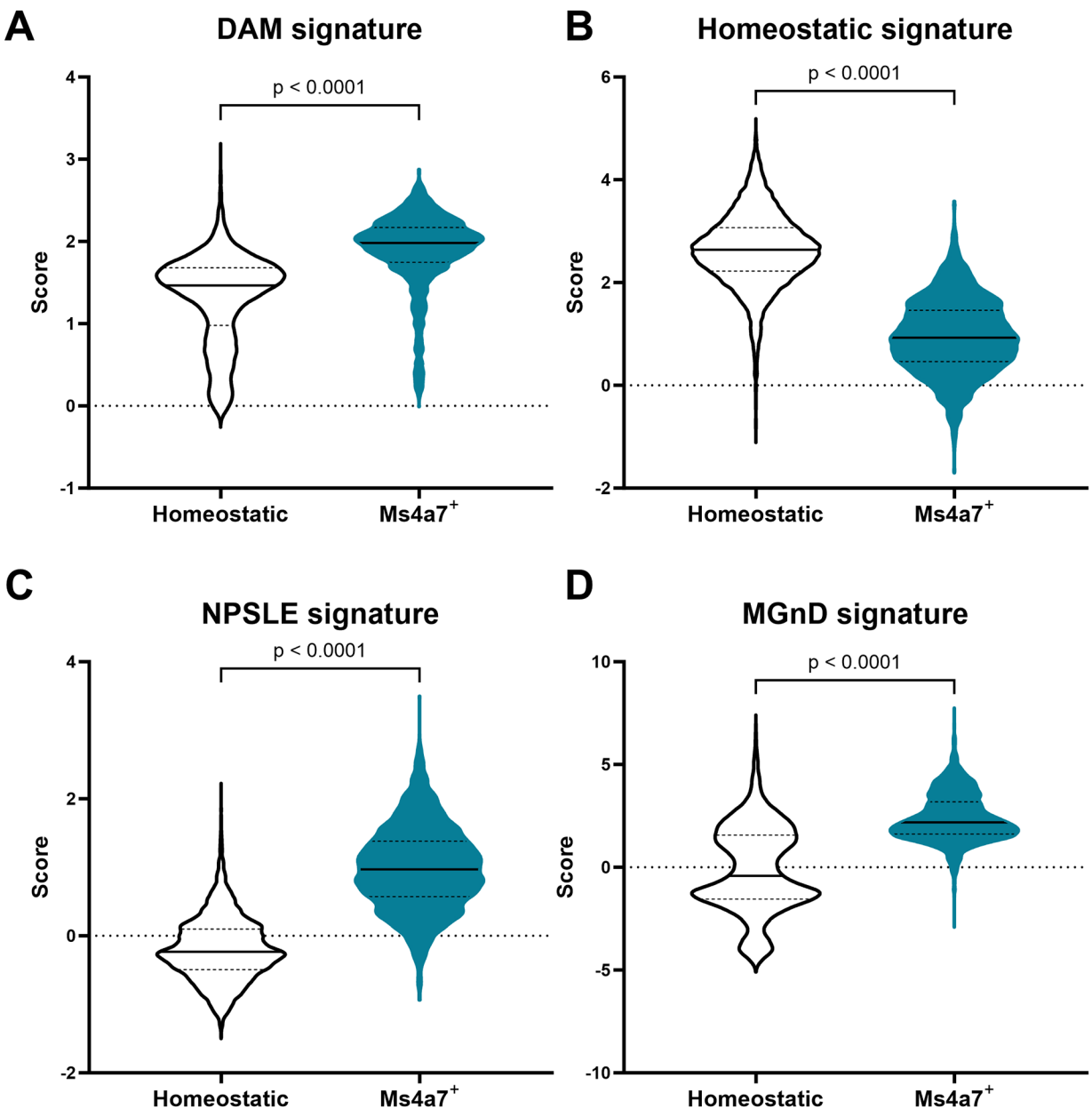

Extended Data Fig. 5 |. Concordance score of Ms4a7+ microglia with microglial gene signatures. **a)** Higher DAM signature gene set score in Ms4a7^{+} compared with Homeostatic microglia (Keren-Shaul et al. (2017)[35] median (solid line) with quartiles (dash); n = 3 mice per group; n = 2515–15285 cells/cluster; two-tailed Mann-Whitney test; $p < 0.0001$). **b)** Lower Homeostatic signature gene set score in Homeostatic compared with Ms4a7^{+} cluster (Keren-Shaul et al.[35]; median (solid line) with quartiles (dash); n = 3 mice per group; n = 2515–15285 cells/cluster; two-tailed Mann-Whitney test; $p < 0.0001$). **c)** Higher NPSLE signature gene set score in Ms4a7^{+} compared with Homeostatic microglia (Makinde et al.[38]; median (solid line) with quartiles (dash); n = 3 mice per group; n = 2515–15285 cells/cluster;

two-tailed Mann-Whitney test; $p < 0.0001$). **d)** Higher MGnD signature gene set score in Ms4a7^{+} compared with Homeostatic microglia (Krasemann et al.[39]; median (solid line) with quartiles (dash); n = 3 mice per group; n = 2515–15285 cells/cluster; two-tailed Mann-Whitney test; $p < 0.0001$).

Extended Data Table 1

ScRNA-seq quality control metrics summary

	DNRAb^{-} 1	DNRAb^{-} 2	DNRAb^{-} 3	DNRAb^{+} 1	DNRAb^{+} 2	DNRAb^{+} 3	DNRAb^{+} capto 1	DNRAb^{+} capto 2	DNRAb^{+} capto 3
Estimated Number of Cells	6119	1868	3092	763	1257	754	2189	1445	2306
Mean Reads per Cell	24574	77412	45456	205512	130434	194448	71837	108980	66490
Median Genes per Cell	2025	2778	2504	2738	2664	2986	2815	2889	2716
Number of Reads	150370974	144605605	140548918	156805849	163955607	146613789	157251130	157476807	153326132
Valid Barcodes	0.977	0.976	0.976	0.975	0.973	0.974	0.977	0.975	0.975
Sequencing Saturation	0.48	0.707	0.595	0.874	0.8	0.86	0.73	0.791	0.696
Q30 Bases in Barcode	0.978	0.978	0.976	0.978	0.978	0.978	0.978	0.976	0.976
Q30. Bases in RNA Read	0.883	0.891	0.882	0.894	0.89	0.887	0.897	0.89	0.88
Q30 Bases in UMI	0.978	0.978	0.974	0.978	0.978	0.978	0.978	0.975	0.974
Reads Mapped to Genome	0.945	0.926	0.939	0.923	0.909	0.921	0.948	0.933	0.936
Reads Mapped Confidently to Genome	0.93	0.91	0.924	0.908	0.893	0.905	0.932	0.917	0.92
Reads Mapped Confidently to Intergenic Regions	0.042	0.044	0.043	0.046	0.047	0.043	0.043	0.042	0.04
Reads Mapped Confidently to Intronic Regions	0.365	0.365	0.378	0.382	0.379	0.384	0.387	0.395	0.392
Reads Mapped Confidently to Exonic Regions	0.522	0.5	0.504	0.48	0.467	0.479	0.503	0.48	0.488
Reads Mapped Confidently to Transcriptome	0.476	0.454	0.457	0.434	0.421	0.433	0.459	0.436	0.446
Reads Mapped	0.026	0.027	0.027	0.027	0.026	0.027	0.024	0.026	0.024

	DNRAb⁻ 1	DNRAb⁻ 2	DNRAb⁻ 3	DNRAb⁺ 1	DNRAb⁺ 2	DNRAb⁺ 3	DNRAb⁺ capto 1	DNRAb⁺ capto 2	DNRAb⁺ capto 3
Antisense to Gene									
Fraction Reads in Cells	0.801	0.773	0.79	0.764	0.77	0.784	0.865	0.847	0.85
Total Genes Detected	18639	17196	17670	15776	17136	16388	17051	17162	17638
Median UMI Counts per Cell	4481	7153	5927	7186	7322	8300	7266	7805	6570

For each sample (n = 3 mice per treatment group), estimated number of cells; mean reads per cell; median genes per cell; number of reads; valid barcodes; sequencing saturation; Q30 bases in barcode, RNA read and UMI; reads mapped to genome; reads mapped confidently to genome, intergenic regions, intronic regions, exonic regions and transcriptome; reads mapped to antisense to gene; fraction of reads in cells; total genes detected; and median UMI counts per cell.

Extended Data Table 2

ScRNA-seq cell cluster composition frequency and percentage

	DNRAb⁻ 1	DNRAb⁻ 2	DNRAb⁻3	DNRAb⁺ 1	DNRAb⁺ 2	DNRAb⁺ 3	DNRAb⁺ capto 1	DNRAb⁺ capto 2	DNRAb⁺ capto 3
Number of cells in Homeostatic cluster	4924	1431	2476	537	709	457	1848	1119	1784
% of total cells	83.13355	80.89316	84.01765	80.63063	64.396	68.92911	89.57828	86.20955	83.40346
Number of cells In Ms4a7+ cluster	741	294	378	93	305	157	131	123	293
% of total cells	12.51055	16.61956	12.8266	13.96396	27.70209	23.68024	6.349976	9.476117	13.69799
Number of cells in Tmem119- cluster	41	17	38	15	50	18	23	33	34
% of total cells	0.692217	0.960995	1.289447	2.252252	4.541326	2.714932	1.114881	2.542373	1.589528
Number of cells In IFN-responsIve cluster	163	15	29	6	7	6	39	15	16
% of total cells	2.751984	0.847937	0.984052	0.900901	0.635786	0.904977	1.890451	1.155624	0.748013
Number of cells in Cycling cluster	44	9	17	10	9	4	18	5	9
% of total cells	0.742867	0.508762	0.576858	1.501502	0.817439	0.603318	0.872516	0.385208	0.420757
Number of cells in	10	3	9	5	21	21	4	3	3

	DNRAb⁻ 1	DNRAb⁻ 2	DNRAb⁻3	DNRAb⁺ 1	DNRAb⁺ 2	DNRAb⁺ 3	DNRAb⁺ capto 1	DNRAb⁺ capto 2	DNRAb⁺ capto 3
S100a4+ cluster									
% of total cells	0.168833	0.169587	0.305395	0.750751	1.907357	3.167421	0.193892	0.231125	0.140252

For each sample (n = 3 mice per treatment group), number of cells in each cluster and the percentage of total cells this represents.

Extended Data Table 3

ScRNA-seq cell cluster comparison statistics

Cluster	Treatment	ANOVA p-value	FDR adjusted p-value	Mean	F statistic	Comparison	Pairwise p-value	Adjusted p-value
Homeostatic	DNRAb⁻			0.82681		DNRAb⁺ vs DNRAb⁻	0.0117396	0.034807
	DNRAb⁺	0.004518	0.01477	0.71319	9.919631	DNRAb⁺ vs DNRAb⁺ capto	0.0016230	0.004861
	DNRAb⁺ Captopril			0.86397		DNRAb⁺ capto vs DNRAb⁻	0.2494213	0.577148
Ms4a7+	DNRAb⁻			0.13986		DNRAb⁺ vs DNRAb⁻	0.0521964	0.148559
	DNRAb⁺	0.013422	0.026844	0.21782	6.948678	DNRAb⁺ vs DNRAb⁺ capto	0.0042981	0.012839
	DNRAb⁺ Captopril			0.09841		DNRAb⁺ capto vs DNRAb⁻	0.1673378	0.422693
Tmem119-	DNRAb⁻			0.00981		DNRAb⁺ vs DNRAb⁻	0.0075268	0.022411
	DNRAb⁺	0.022958	0.034437	0.03169	5.712187	DNRAb⁺ vs DNRAb⁺ capto	0.0770633	0.213831
	DNRAb⁺ Captopril			0.01749		DNRAb⁺ capto vs DNRAb⁻	0.1971263	0.482463
IFN-responsive	DNRAb⁻			0.01528		DNRAb⁺ vs DNRAb⁻	0.2552766	0.058696
	DNRAb⁺	0.488584	0.488584	0.00814	0.771867	DNRAb⁺ vs DNRAb⁺ capto	0.4146736	0.799463
	DNRAb⁺ captopril			0.01265		DNRAb⁺ capto vs DNRAb⁻	0.7287750	0.980048
Cycling	DNRAb⁻			0.00609		DNRAb⁺ vs DNRAb⁻	0.3495265	0.724774
	DNRAb⁺	0.466644	0.488584	0.00974	0.82538	DNRAb⁺ vs DNRAb⁺ capto	0.2556850	0.587645

Cluster	Treatment	ANOVA p-value	FDR adjusted p-value	Mean	F statistic	Comparison	Pairwise p-value	Adjusted p-value
	DNRAb$^+$ captopril			0.00559		DNRAb$^+$ capto vs DNRAb$^-$	0.8266030	0.994787
	DNRAb$^-$			0.00214		DNRAb$^+$ vs DNRAb$^-$	0.0039998	0.011952
S100a4+	DNRAb$^+$	0.004923	0.01477	0.01942	9.660058	DNRAb$^+$ vs DNRAb$^+$ capto	0.0033397	0.009985
	DNRAb$^+$ captopril			0.00188		DNRAb$^+$ capto vs DNRAb$^-$	0.9129096	0.999339

For each cluster, ANOVA *P* value, FDR-adjusted *P* value, means of the groups compared and *F* statistic are reported (n = 3 mice per treatment group). Post-hoc, pairwise Student's *t*-tests were performed between each treatment group within each cluster; comparisons performed, pairwise *P* values and Holm-Šídák-adjusted *P* values are reported (n = 3 mice per treatment group).

Extended Data Table 4

ScRNA-seq gene expression in Ms4a7$^+$ cluster by samplea

1Gene	DNRAb$^-$ 1	DNRAb$^-$ 2	DNRAb$^-$ 3	DNRAb$^+$ 1	DNRAb$^+$ 2	DNRAb$^+$ 3	DNRAb$^+$ capto 1	DNRAb$^+$ capto 2	DNRAb$^+$ capto 3
Tnf									
TPM	78.75947	136.7593	119.0401	130.1744	139.7316	162.5265	44.29625	65.39778	154.4324
Log_2TPM	6.317584	7.106006	6.907372	7.035343	7.136802	7.353381	5.50132	6.053063	7.280143
Il1b									
TPM	125.6192	285.5573	69.24553	147.6606	269.6664	540.32	18.79235	117.716	233.2621
Log_2TPM	6.984352	8.16268	6.134335	7.215878	8.080372	9.080338	4.306871	6.891371	7.87198
C3ar1									
TPM	405.4573	352.4923	369.1798	462.4107	443.4286	433.7629	408.0625	417.2378	420.4249
Log_2TPM	8.66696	8.465535	8.532082	8.856147	8.795808	8.764085	8.676177	8.70818	8.719132
Lyz2									
TPM	7777.828	7907.481	7644.24	9634.851	9430.076	10136.92	6151.81	9920.843	7553.358
Log_2TPM	12.92534	12.94918	12.90035	13.2342	13.20321	13.30747	12.58703	13.27639	12.88309
Ifnar1									
TPM	152.459	178.6539	150.1617	172.9183	194.9023	213.1143	167.7888	164.8024	109.2552
Log_2TPM	7.261709	7.489076	7.239948	7.442266	7.613991	7.742237	7.399076	7.373321	6.784702
Cd93									
TPM	150.039	154.5765	175.837	178.747	199.5429	172.2136	157.0504	187.0376	85.74455
Log_2TPM	7.238777	7.281481	7.466276	7.489824	7.647767	7.436408	7.30424	7.554878	6.438701

1Gene	DNRAb⁻ 1	DNRAb⁻ 2	DNRAb⁻ 3	DNRAb⁺ 1	DNRAb⁺ 2	DNRAb⁺ 3	DNRAb⁺ capto 1	DNRAb⁺ capto 2	DNRAb⁺ capto 3
Axl									
TPM	129.3591	152.1688	141.2142	114.6312	183.5588	220.6486	130.2041	198.8092	123.5459
Log_2TPM	7.026348	7.258979	7.151922	6.853387	7.527937	7.792131	7.035669	7.642479	6.960534
Lairl									
TPM	439.7771	422.7982	430.645	415.781	407.8512	389.6332	437.5933	395.0026	441.6305
Log_2TPM	8.783905	8.727234	8.753701	8.703146	8.675432	8.609671	8.77674	8.629366	8.789959
Il10									
TPM	9.0199	2.4077	5.4462	3.8858	37.1242	21.5266	1.3423	26.1591	6.9148
Log_2TPM	3.173117	1.267676	2.445270	1.958213	5.214290	4.428054	0.424718	4.709241	2.789704

For each sample (n = 3 mice per treatment group), TPM and $\log_2$(TPM) for each indicated gene (*Tnf, Il1b, C3ar1, Lyz2, Ifnar1, Cd93, Axl, Lair1* and *Il10*).

Extended Data Table 5

ScRNA-seq Ms4a7⁺ cell gene expression comparison statistics

Gene	Comparison	logFC	logCPM	LR	p-value	padj
Tnf	DNRAb⁺ vs DNRAb⁻	0.475008	6.977014	6.651073	0.00991	0.151184
	DNRAb⁺ vs DNRAb⁺ capto	0.756772	6.935088	5.489881	0.019127	0.32575
	DNRAb⁺ capto vs DNRAb⁻	−0.29284	6.696582	0.733314	0.391811	0.993521
Il1b	DNRAb⁺ vs DNRAb⁻	1.092901	7.897332	6.787678	0.009179	0.143578
	DNRAb⁺ vs DNRAb⁺ capto	1.467294	7.871111	5.907503	0.015077	0.287376
	DNRAb⁺ capto vs DNRAb⁻	−0.36953	7.197758	0.343762	0.557666	0.993521
C3ar1	DNRAb⁺ vs DNRAb⁻	0.32206	8.688049	7.359287	0.006672	0.116852
	DNRAb⁺ vs DNRAb⁺ capto	0.154019	8.78866	0.790979	0.373804	0.892005
	DNRAb⁺ capto vs DNRAb⁻	0.179949	8.638248	1.250056	0.263542	0.993521
Lyz2	DNRAb⁺ vs DNRAb⁻	0.403402	13.11144	12.55886	0.000394	0.015454
	DNRAb⁺ vs DNRAb⁺ capto	0.345297	13.14444	2.232687	0.135119	0.701726
	DNRAb⁺ capto vs DNRAb⁻	0.069946	12.95071	0.097732	0.754569	0.998601
Ifnar1	DNRAb⁺ vs DNRAb⁻	0.37003	7.470336	7.467909	0.006281	0.111822
	DNRAb⁺ vs DNRAb⁺ capto	0.465003	7.461662	4.029725	0.044705	0.475877
	DNRAb⁺ capto vs DNRAb⁻	−0.09564	7.275785	0.190183	0.662764	0.993521
Cd93	DNRAb⁺ vs DNRAb⁻	0.295406	7.430908	5.597676	0.017984	0.21385
	DNRAb⁺ vs DNRAb⁺ capto	0.410382	7.39705	2.13733	0.143752	0.71292
	DNRAb⁺ capto vs DNRAb⁻	−0.11804	7.253963	0.183124	0.668702	0.993521
Axl	DNRAb⁺ vs DNRAb⁻	0.417811	7.310917	5.867303	0.015425	0.193616

Gene	Comparison	logFC	logCPM	LR	p-value	padj
	DNRAb$^+$ vs DNRAb$^+$ capto	0.267126	7.402549	0.919316	0.337655	0.876081
	DNRAb$^+$ capto vs DNRAb$^-$	0.137412	7.193658	0 380254	0.537467	0.993521
	DNRAb$^+$ vs DNRAb$^-$	−0.01522	8.720331	0.018162	0.892797	0.979846
Lair1	DNRAb$^+$ vs DNRAb$^+$ capto	−0.01919	8.731565	0.012642	0.910478	0.991134
	DNRAb$^+$ capto vs DNRAb$^-$	0.013904	8.752519	0.008258	0.927592	0.998601
	DNRAb$^+$ vs DNRAb$^-$	2.02383254	3.77062569	19.1498946	1.2084E-05	0.00104459
Il10	DNRAb$^+$ vs DNRAb$^+$ capto	0.98379857	4.32117111	1.87798668	0.17056315	0.75062606
	DNRAb$^+$ capto vs DNRAb$^-$	1.01742024	3.072002	2.0948237	0.14779876	0.98088697

For each gene, comparisons between each group were performed using a Likelihood ratio test with FDR and Benjamini-Hochberg corrections. The log(FC), log(counts per min), likelihood ratio, *P* value and adjusted *P* value (P_{adj}) are reported (n = 3 mice per treatment group).

Supplementary Material

Refer to Web version on PubMed Central for supplementary material.

Acknowledgements

We thank R. A. Berlin and H. Khalili for their technical assistance. We also thank Y. Atisha-Fregoso, M. Lesser, R. Rasul, H. Rahman and C. Chuizan for their statistical expertise. The present study was supported by grants from the National Institutes of Health (NIH grant no. 1P01AI073693) to B.D. and J.Z.L.

Data availability

The accession no. for the sequencing data reported in the present study is Gene Expression Omnibus (GEO) GSE230077 and can also be accessed through a single-cell portal, accession no. SCP2193. Previously published datasets used in identifying and naming clusters are publicly available: Allen Brain Atlas, GEO accession nos. GSE121654 and GSE152184. Previously published datasets used for microglial comparisons are publicly available at: GEO, accession no. GSE98971; Mendeley Data (1, 2): GEO accession no. GSE101689.

References

1. Kello N, Anderson E & Diamond B Cognitive dysfunction in systemic lupus erythematosus: a case for initiating trials. Arthritis Rheumatol. 71, 1413–1425 (2019). [PubMed: 31102496]
2. Mackay M et al. Brain metabolism and autoantibody titres predict functional impairment in systemic lupus erythematosus. Lupus Sci. Med 2, e000074 (2015). [PubMed: 25861456]
3. Mackay M et al. Metabolic and microstructural alterations in the SLE brain correlate with cognitive impairment. JCI Insight 4, e124002 (2019). [PubMed: 30626758]
4. Kowal C et al. Cognition and immunity: antibody impairs memory. Immunity 21, 179–188 (2004). [PubMed: 15308099]
5. Degiorgio LA et al. A subset of lupus anti-DNA antibodies cross-reacts with the NR2 glutamate receptor in systemic lupus erythematosus. Nat. Med. 7, 1189–1193 (2001). [PubMed: 11689882]
6. Tay SH, Fairhurst AM & Mak A Clinical utility of circulating anti-N-methyl-d-aspartate receptor subunits NR2A/B antibody for the diagnosis of neuropsychiatric syndromes in systemic lupus

erythematosus and Sjögren's syndrome: an updated meta-analysis. Autoimmun. Rev. 16, 114–122 (2017). [PubMed: 27988431]

7. Kowal C et al. Human lupus autoantibodies against NMDA receptors mediate cognitive impairment. Proc. Natl Acad. Sci. USA 103, 19854–19859 (2006). [PubMed: 17170137]
8. Arinuma Y, Yanagida T & Hirohata S Association of cerebrospinal fluid anti-NR2 glutamate receptor antibodies with diffuse neuropsychiatric systemic lupus erythematosus. Arthritis Rheum. 58, 1130–1135 (2008). [PubMed: 18383393]
9. Putterman C & Diamond B Immunization with a peptide surrogate for double-stranded DNA (dsDNA) induces autoantibody production and renal immunoglobulin deposition. J. Exp. Med. 188, 29–38 (1998). [PubMed: 9653081]
10. Chang EH et al. Selective impairment of spatial cognition caused by autoantibodies to the *N*-methyl-d-aspartate receptor. eBioMedicine 2, 755–764 (2015). [PubMed: 26286205]
11. Chan K et al. Lupus autoantibodies act as positive allosteric modulators at GluN2A-containing NMDA receptors and impair spatial memory. Nat. Commun. 11, 1403 (2020). [PubMed: 32179753]
12. Nestor J et al. Lupus antibodies induce behavioral changes mediated by microglia and blocked by ACE inhibitors. J. Exp. Med. 215, 2554–2566 (2018). [PubMed: 30185634]
13. Maroso M et al. Toll-like receptor 4 and high-mobility group box-1 are involved in ictogenesis and can be targeted to reduce seizures. Nat. Med. 16, 413–419 (2010). [PubMed: 20348922]
14. Pedrazzi M et al. Potentiation of NMDA receptor-dependent cell responses by extracellular high mobility group box 1 protein. PLoS ONE 7, e44518 (2012). [PubMed: 22952988]
15. Tanaka H et al. HMGB1 signaling phosphorylates Ku70 and impairs DNA damage repair in Alzheimer's disease pathology. Commun. Biol. 4, 1175 (2021). [PubMed: 34635772]
16. Balosso S, Liu J, Bianchi ME & Vezzani A Disulfide-containing high mobility group box-1 promotes *N*-methyl-d-aspartate receptor function and excitotoxicity by activating Toll-like receptor 4-dependent signaling in hippocampal neurons. Antioxid. Redox Signal. 21, 1726–1740 (2014). [PubMed: 24094148]
17. Schafer DP et al. Microglia sculpt postnatal neural circuits in an activity and complement-dependent manner. Neuron 74, 691–705 (2012). [PubMed: 22632727]
18. Mazarati A, Maroso M, Iori V, Vezzani A & Carli M High-mobility group box-1 impairs memory in mice through both toll-like receptor 4 and receptor for advanced glycation end products. Exp. Neurol. 232, 143–148 (2011). [PubMed: 21884699]
19. Liu T, Son M & Diamond B HMGB1 in systemic lupus erythematosus. Front. Immunol. 11, 1057 (2020). [PubMed: 32536928]
20. Son M et al. C1q and HMGB1 reciprocally regulate human macrophage polarization. Blood 128, 2218–2228 (2016). [PubMed: 27683415]
21. Wilton DK et al. Microglia and complement mediate early corticostriatal synapse loss and cognitive dysfunction in Huntington's disease. Nat. Med. 29, 2866–2884 (2023). [PubMed: 37814059]
22. Esen N & Kielian T Effects of low dose GM-CSF on microglial inflammatory profiles to diverse pathogen-associated molecular patterns (PAMPs). J. Neuroinflam. 4, 10 (2007).
23. Paudel YN et al. Impact of HMGB1, RAGE, and TLR4 in Alzheimer's disease (AD): from risk factors to therapeutic targeting. Cells 9, 383 (2020). [PubMed: 32046119]
24. Fang P, Schachner M & Shen YQ HMGB1 in development and diseases of the central nervous system. Mol. Neurobiol. 45, 499–506 (2012). [PubMed: 22580958]
25. Andersson U, Yang H & Harris H Extracellular HMGB1 as a therapeutic target in inflammatory diseases. Expert Opin. Ther. Targets 22, 263–277 (2018). [PubMed: 29447008]
26. Khalil M, Inaba K, Steinman R, Ravetch J & Diamond B T cell studies in a peptide-induced model of systemic lupus erythematosus. J. Immunol. 166, 1667–1674 (2001). [PubMed: 11160209]
27. Zhang J et al. Polyreactive autoantibodies in systemic lupus erythematosus have pathogenic potential. J. Autoimmun. 33, 270–274 (2009). [PubMed: 19398190]

28. Liu T et al. HMGB1-C1q complexes regulate macrophage function by switching between leukotriene and specialized proresolving mediator biosynthesis. Proc. Natl Acad. Sci. USA 116, 23254–23263 (2019). [PubMed: 31570601]
29. Stevens B et al. The classical complement cascade mediates CNS synapse elimination. Cell 131, 1164–1178 (2007). [PubMed: 18083105]
30. Stephan AH, Barres BA & Stevens B The complement system: an unexpected role in synaptic pruning during development and disease. Annu Rev. Neurosci. 35, 369–389 (2012). [PubMed: 22715882]
31. Stephan AH et al. A dramatic increase of C1q protein in the CNS during normal aging. J. Neurosci. 33, 13460–13474 (2013). [PubMed: 23946404]
32. Gazestani V et al. Early Alzheimer's disease pathology in human cortex involves transient cell states. Cell 186, 4438–4453 e4423 (2023). [PubMed: 37774681]
33. Hammond TR et al. Single-cell RNA sequencing of microglia throughout the mouse lifespan and in the injured brain reveals complex cell-state changes. Immunity 50, 253–271 e256 (2019). [PubMed: 30471926]
34. Mercurio D et al. Protein expression of the microglial marker Tmem119 decreases in association with morphological changes and location in a mouse model of traumatic brain injury. Front. Cell Neurosci. 16, 820127 (2022). [PubMed: 35221925]
35. Keren-Shaul H et al. A unique microglia type associated with restricting development of Alzheimer's disease. Cell 169, 1276–1290.e1217 (2017). [PubMed: 28602351]
36. Ruan C & Elyaman W A new understanding of TMEM119 as a marker of microglia. Front. Cell Neurosci. 16, 902372 (2022). [PubMed: 35769325]
37. Paolicelli RC et al. Microglia states and nomenclature: a field at its crossroads. Neuron 110, 3458–3483 (2022). [PubMed: 36327895]
38. Makinde HM et al. A novel microglia-specific transcriptional signature correlates with behavioral deficits in neuropsychiatric lupus. Front. Immunol. 11, 230 (2020). [PubMed: 32174913]
39. Krasemann S et al. The TREM2-APOE pathway drives the transcriptional phenotype of dysfunctional microglia in neurodegenerative diseases. Immunity 47, 566–581.e569 (2017). [PubMed: 28930663]
40. Seliga A et al. Kallikrein-kinin system suppresses type I interferon responses: a novel pathway of interferon regulation. Front. Immunol. 9, 156 (2018). [PubMed: 29456540]
41. Jackson L, Eldahshan W, Fagan S & Ergul A Within the brain: the renin angiotensin system. Int. J. Mol. Sci. 19, 876 (2018). [PubMed: 29543776]
42. Noda M et al. Neuroprotective role of bradykinin because of the attenuation of pro-inflammatory cytokine release from activated microglia. J. Neurochem. 101, 397–410 (2007). [PubMed: 17402969]
43. Nocito C et al. Centrally acting angiotensin-converting enzyme inhibitor suppresses type i interferon responses and decreases inflammation in the periphery and the CNS in lupus-prone mice. Front. Immunol. 11, 573677 (2020). [PubMed: 33042154]
44. Carvalheiro T et al. Leukocyte associated immunoglobulin like receptor 1 regulation and function on monocytes and dendritic cells during inflammation. Front. Immunol. 11, 1793 (2020). [PubMed: 32973751]
45. Huang Y, Smith DE, Ibanez-Sandoval O, Sims JE & Friedman WJ Neuron-specific effects of interleukin-1beta are mediated by a novel isoform of the IL-1 receptor accessory protein. J. Neurosci. 31, 18048–18059 (2011). [PubMed: 22159118]
46. Vo A et al. Regional brain metabolism in a murine systemic lupus erythematosus model. J. Cereb. Blood Flow. Metab. 34, 1315–1320 (2014). [PubMed: 24824914]
47. Fujita K et al. HMGB1, a pathogenic molecule that induces neurite degeneration via TLR4-MARCKS, is a potential therapeutic target for Alzheimer's disease. Sci. Rep. 6, 31895 (2016). [PubMed: 27557632]
48. Lecca D et al. Role of chronic neuroinflammation in neuroplasticity and cognitive function: a hypothesis. Alzheimers Dement. 18, 2327–2340 (2022). [PubMed: 35234334]
49. Chavan SS et al. HMGB1 mediates cognitive impairment in sepsis survivors. Mol. Med. 18, 930–937 (2012). [PubMed: 22634723]

50. Zaghloul N et al. Forebrain cholinergic dysfunction and systemic and brain inflammation in murine sepsis survivors. Front. Immunol. 8, 1673 (2017). [PubMed: 29326685]
51. Son M, Diamond B & Shin JS Editorial: The role of HMGB1 in immunity. Front. Immunol. 11, 594253 (2020). [PubMed: 33013940]
52. Tamburini B et al. Emerging roles of cells and molecules of innate immunity in Alzheimer's disease. Int. J. Mol. Sci. 24, 11922 (2023). [PubMed: 37569296]
53. Salter MW & Stevens B Microglia emerge as central players in brain disease. Nat. Med. 23, 1018–1027 (2017). [PubMed: 28886007]
54. Hammond TR, Marsh SE & Stevens B Immune signaling in neurodegeneration. Immunity 50, 955–974 (2019). [PubMed: 30995509]
55. Eyo U & Molofsky AV Defining microglial-synapse interactions. Science 381, 1155–1156 (2023). [PubMed: 37708287]
56. Zou J & Crews FT Glutamate/NMDA excitotoxicity and HMGB1/TLR4 neuroimmune toxicity converge as components of neurodegeneration. AIMS Mol. Sci. 2, 77–100 (2015).
57. Labandeira-Garcia JL et al. Brain renin–angiotensin system and microglial polarization: implications for aging and neurodegeneration. Front. Aging Neurosci. 9, 129 (2017). [PubMed: 28515690]
58. Yang XF et al. Myeloid angiotensin II type 1 receptor mediates macrophage polarization and promotes vascular injury in DOCA/salt hypertensive mice. Front. Pharm. 13, 879693 (2022).
59. Cao L et al. Angiotensin II upregulates fibroblast-myofibroblast transition through Cx43-dependent CaMKII and TGF-beta1 signaling in neonatal rat cardiac fibroblasts. Acta Biochim Biophys. Sin. (Shanghai) 50, 843–852 (2018). [PubMed: 30060053]
60. Quitterer U & AbdAlla S Improvements of symptoms of Alzheimer's disease by inhibition of the angiotensin system. Pharmacol. Res. 154, 104230 (2020). [PubMed: 30991105]
61. Nagy A et al. The correlation between two angiotensin-converting enzyme inhibitors' concentrations and cognition. Int. J. Environ. Res Public Health 19, 14375 (2022). [PubMed: 36361252]
62. Ghalayini J & Boulianne GL Deciphering mechanisms of action of ACE inhibitors in neurodegeneration using *Drosophila* models of Alzheimer's disease. Front. Neurosci. 17, 1166973 (2023). [PubMed: 37113150]
63. O'Caoimh R et al. Effects of centrally acting angiotensin converting enzyme inhibitors on functional decline in patients with Alzheimer's disease. J. Alzheimers Dis. 40, 595–603 (2014). [PubMed: 24496072]
64. Ichinose K et al. Predictors of clinical outcomes in patients with neuropsychiatric systemic lupus erythematosus. Cytokine 79, 31–37 (2016). [PubMed: 26745468]
65. Faust TW et al. Neurotoxic lupus autoantibodies alter brain function through two distinct mechanisms. Proc. Natl Acad. Sci. USA 107, 18569–18574 (2010). [PubMed: 20921396]
66. Santiago TC et al. Angiotensin-converting enzymes as druggable features of psychiatric and neurodegenerative disorders. J. Neurochem. 10.1111/jnc.15806 (2023).
67. Badimon A et al. Negative feedback control of neuronal activity by microglia. Nature 586, 417–423 (2020). [PubMed: 32999463]

References

68. Bordt EA et al. Isolation of microglia from mouse or human tissue. STAR Protoc. 10.1016/j.xpro.2020.100035 (2020).
69. Zheng GX et al. Massively parallel digital transcriptional profiling of single cells. Nat. Commun. 8, 14049 (2017). [PubMed: 28091601]
70. Lun ATL et al. EmptyDrops: distinguishing cells from empty droplets in droplet-based single-cell RNA sequencing data. Genome Biol. 20, 63 (2019). [PubMed: 30902100]
71. Hao Y et al. Integrated analysis of multimodal single-cell data. Cell 184, 3573–3587.e3529 (2021). [PubMed: 34062119]

72. Bais AS & Kostka D scds: computational annotation of doublets in single-cell RNA sequencing data. Bioinformatics 36, 1150–1158 (2020). [PubMed: 31501871]

73. Marsh SE et al. Dissection of artifactual and confounding glial signatures by single-cell sequencing of mouse and human brain. Nat. Neurosci. 25, 306–316 (2022). [PubMed: 35260865]

74. Phipson B et al. propeller: testing for differences in cell type proportions in single cell data. Bioinformatics 38, 4720–4726 (2022). [PubMed: 36005887]

75. Lun ATL & Marioni JC Overcoming confounding plate effects in differential expression analyses of single-cell RNA-seq data. Biostatistics 18, 451–464 (2017). [PubMed: 28334062]

76. Robinson MD, McCarthy DJ & Smyth GK edgeR: a Bioconductor package for differential expression analysis of digital gene expression data. Bioinformatics 26, 139–140 (2010). [PubMed: 19910308]

77. Strimmer K fdrtool: a versatile R package for estimating local and tail area-based false discovery rates. Bioinformatics 24, 1461–1462 (2008). [PubMed: 18441000]

78. Korotkevich G et al. Fast gene set enrichment analysis. Preprint at bioRxiv 10.1101/060012 (2021).

79. Korsunsky I, Nathan A, Millard N & Raychaudhuri S Presto scales Wilcoxon and auROC analyses to millions of observations. Preprint at bioRxiv 10.1101/653253 (2019).

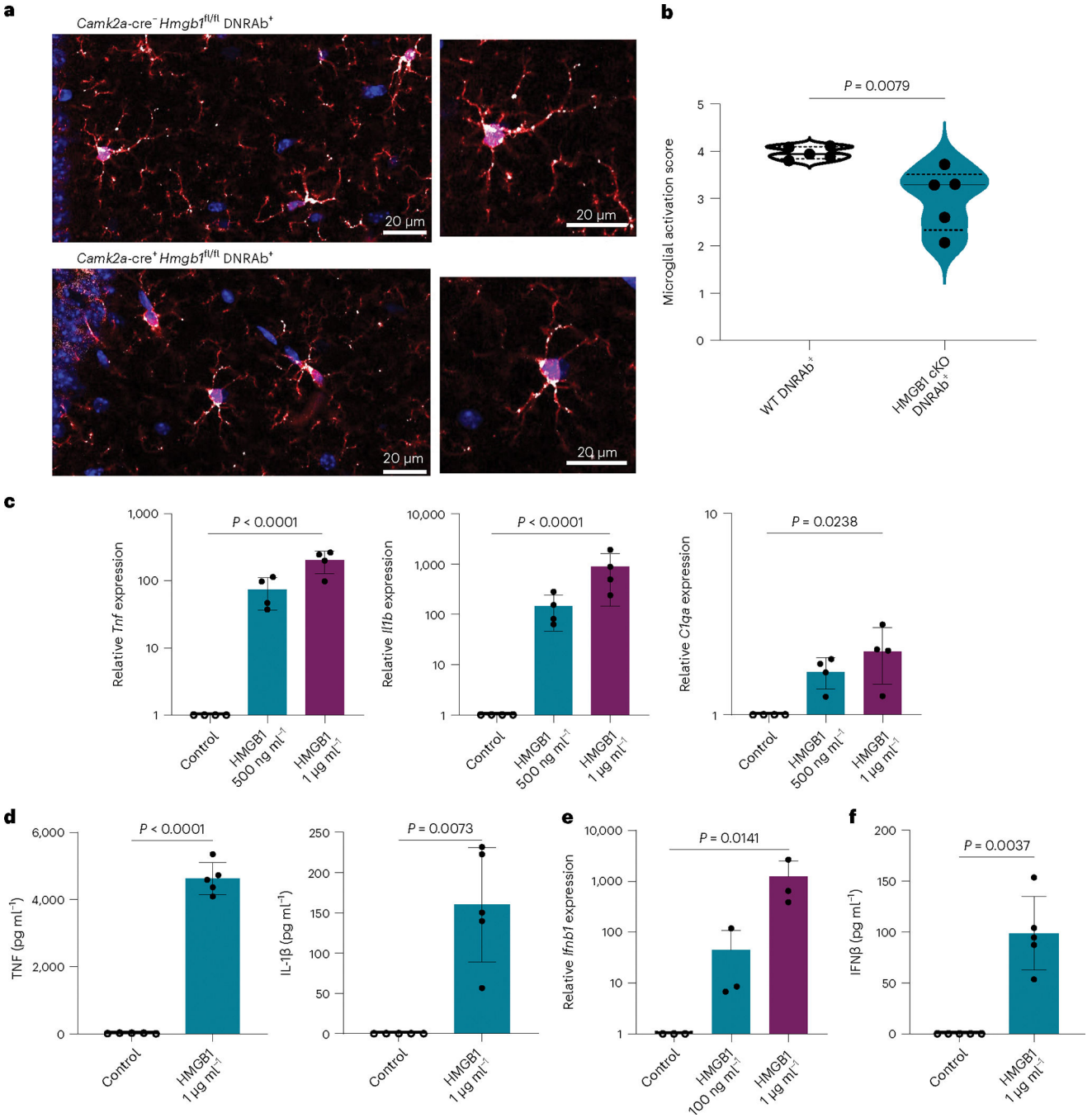

Fig. 1 |. Microglia are activated by neuronal HMGB1.

a, Representative sections of microglia in CA1 stratum radiatum stained for Iba1 (red) and CD68 (white) in *Camk2a*-cre^{-}*Hmgb1*$^{fl/fl}$ B6.H2^{d} DNRAb^{+} mice (WT; $n = 5$, top) and *Camk2a*-cre^{+}*Hmgb1*$^{fl/fl}$ B6.H2^{d} DNRAb^{+} mice (HMGB1 cKO; $n = 5$, bottom). **b**, Decreased activation score in microglia from *Camk2a*-cre^{+}*Hmgb1*$^{fl/fl}$ B6.H2^{d} (HMGB1 cKO) DNRAb^{+} mice compared with *Camk2a*-cre^{-}*Hmgb1*$^{fl/fl}$ B6.H2^{d} (WT) DNRAb^{+} mice based on morphology and CD68 expression (median (solid line) with quartiles (dash); $n = 5$ mice per group; $n = 7$–18 microglia scored per mouse; two-tailed Mann–Whitney

U-test: $P = 0.0079$). **c**, Relative mRNA expression of *Tnf*, *Il1b* and *C1qa* increased with HMGB1 stimulation in cultured WT (B6) microglia stimulated with 0, 500 or 1,000 ng ml^{-1} of HMGB1 for 4.5 h in serum-free medium (mean ± s.d.; microglia cultured from four independent litters; two-tailed, one-way, repeated-measure ANOVA on log transformed data: $P < 0.0001$ (*Tnf*), $P < 0.0001$ (*Il1b*) and $P = 0.0238$ (*C1qa*)). **d**, Secretion of TNF and IL-1β increased with HMGB1 stimulation in cultured WT (B6) microglia stimulated with and without 1 μg ml^{-1} of HMGB1 for 24 h in serum-free medium (mean ± s.d.; microglia cultured from five independent litters; two-tailed, paired Student's *t*-test: $P < 0.0001$ (TNF) and $P = 0.0073$ (IL-1β)). **e**, Relative mRNA expression of *Ifnb1* increased with HMGB1 stimulation in cultured WT (B6) microglia stimulated with 0, 100 or 1,000 ng ml^{-1} of HMGB1 for 4.5 h in serum-free medium (mean ± s.d.; microglia cultured from three independent litters; two-tailed, one-way, repeated-measure ANOVA on log transformed data: $P = 0.0141$). **f**, Secretion of IFN-β increased with HMGB1 stimulation in cultured WT (B6) microglia stimulated with and without 1 μg ml^{-1} of HMGB1 for 24 h in serum-free medium (mean ± s.d.; microglia cultured from five independent litters; two-tailed, paired Student's *t*-test: $P = 0.0037$).

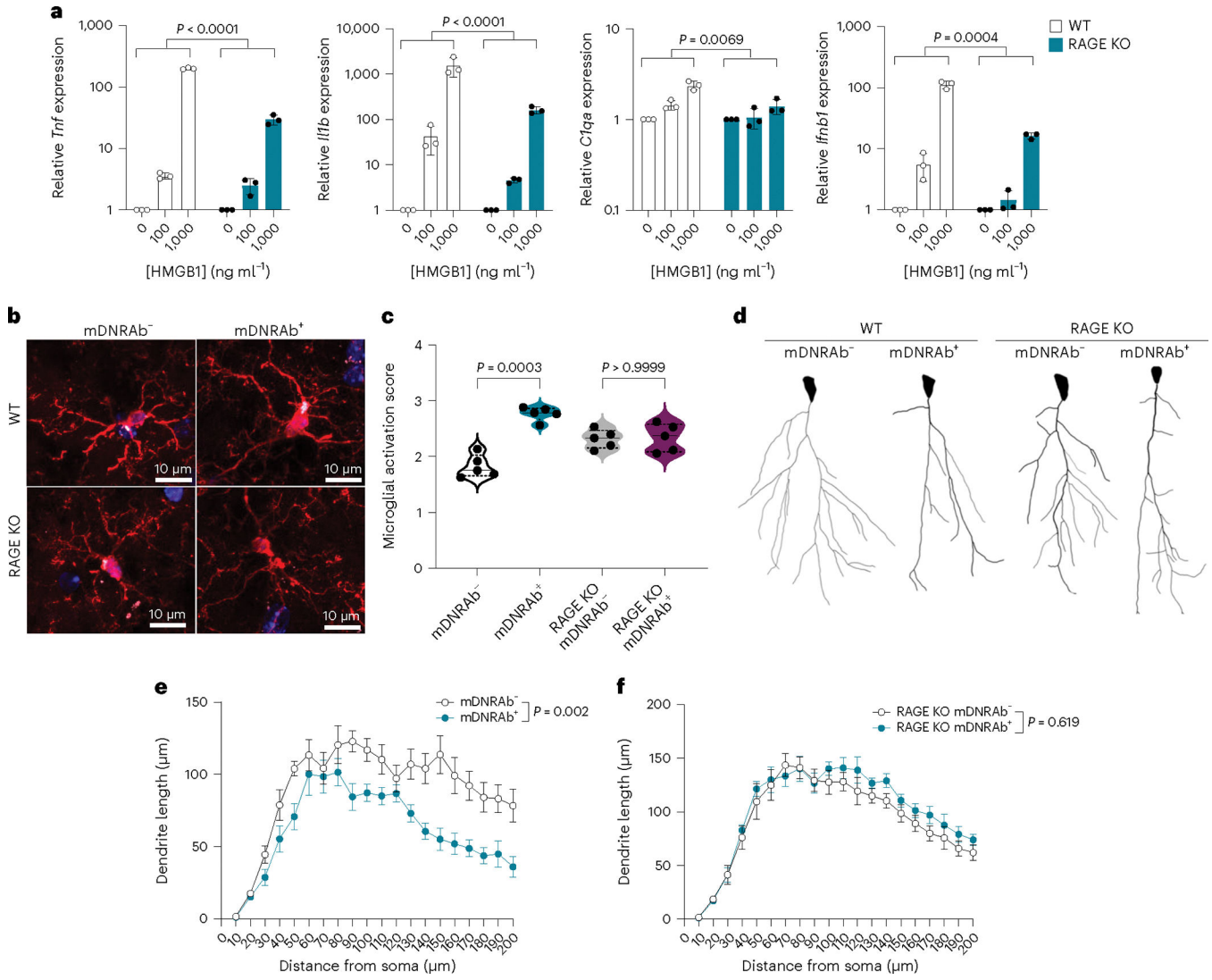

Fig. 2 |. DNRAbs induce microglial activation through RAGE.

a, Loss of RAGE decreased the relative mRNA expression of *Tnf*, *Il1b*, *C1qa* and *Ifnb1* with HMGB1 stimulation compared with WT (B6) microglia. WT and RAGE KO microglia were stimulated with 0, 100 or 1,000 ng ml^{-1} of HMGB1 for 4.5 h in serum-free medium (mean ± s.d.; microglia were cultured from three independent litters; two-tailed, two-way, repeated-measure ANOVA on log transformed data: $P < 0.0001$ (*Tnf*), $P < 0.0001$ (*Il1b*), $P = 0.0069$ (*C1qa*) and $P = 0.0004$ (*Ifnb1*)). **b**, Representative sections of microglia in CA1 stratum radiatum stained for Iba1 (red) and CD68 (white) in WT (B6) and RAGE KO mDNRAb$^-$ (left) and mDNRAb$^+$(right) mice ($n = 5$ mice per group). **c**, Increased activation score in microglia in DNRAb$^+$ WT B6 ($P = 0.0003$) but not RAGE KO mice ($P > 0.9999$) compared with DNRAb$^-$ counterparts based on morphology and CD68 expression (median (solid line) with quartiles (dash); $n = 5$ mice per group; $n = 10$–24 microglia scored per mouse; two-tailed Kruskal–Wallis test). **d**, Representative tracings of CA1 pyramidal neurons from mDNRAb$^-$ and mDNRAb$^+$ in WT B6 and RAGE KO mice. **e**, Analysis of dendritic complexity showed a decrease in WT B6 mDNRAb$^+$ compared with mDNRAb$^-$

groups (mean ± s.e.m.; $n = 7$ mice per group; $n = 25$ neurons analyzed per group; two-tailed, linear mixed model test with Tukey's adjustment: $P = 0.002$). **f**, Analysis of dendritic complexity showed no difference in RAGE KO mDNRAb^{+} compared with mDNRAb^{-} groups (mean ± s.e.m.; $n = 6$–7 mice per group; $n = 24$ neurons analyzed per group; two-sided, linear mixed model test with Tukey's adjustment: $P = 0.619$).

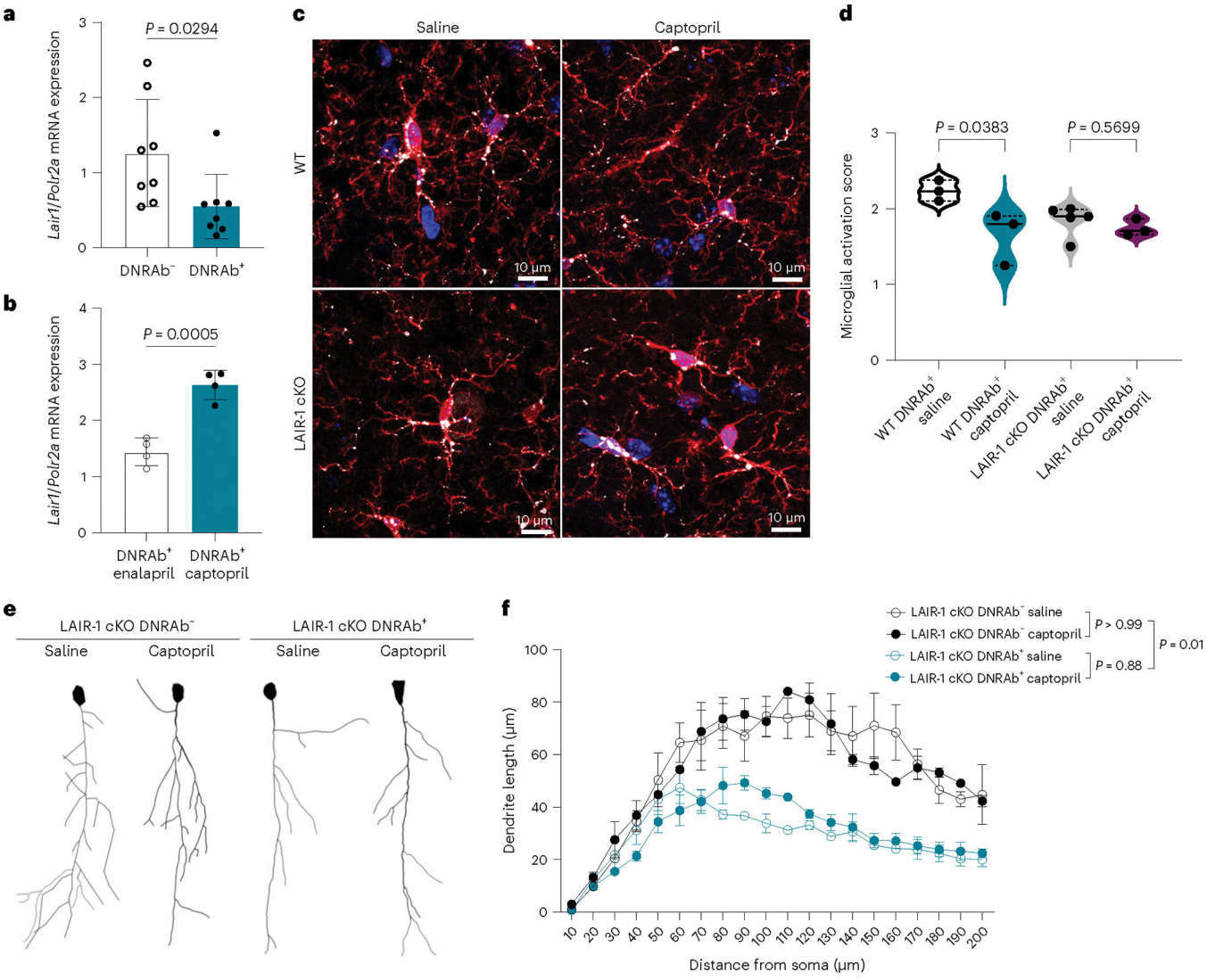

Fig. 3 |. Treatment with ACE inhibitors requires LAIR-1 for efficacy.

a, Decreased *Lair1* mRNA expression in microglia isolated from DNRAb$^+$ compared with DNRAb$^-$ B6.H2^d mice (mean ± s.d.; $n = 8$ mice per group, pooled from two independent experiments; two-tailed, unpaired Student's *t*-test: $P = 0.0294$). **b**, *Lair1* mRNA expression in microglia isolated from DNRAb$^+$ B6.H2^d mice increased in mice treated with captopril (5 mg kg^{-1} i.p.) compared with those treated with enalapril (5 mg kg^{-1} i.p.) daily for 2 weeks (mean ± s.d.; $n = 4$ mice per group; two-tailed, unpaired Student's *t*-test: $P = 0.0005$). **c**, Representative sections of microglia in CA1 stratum radiatum stained for Iba1 (red) and CD68 (white) in DNRAb$^+$ WT (B6.H2^d) and LAIR-1 cKO DNRAb$^-$ mice treated with saline (left) or captopril (5 mg kg^{-1}, right; $n = 3$–5 mice per group). **d**, Decreased activation score in DNRAb$^+$ microglia in WT B6.H2^d ($P = 0.0383$) but not LAIR-1 cKO ($P = 0.5699$) mice treated with captopril compared with saline-treated counterparts based on morphology and CD68 expression (median (solid line) with quartiles (dash); $n = 3$–5 mice per group; $n = 12$–78 microglia scored per mouse; two-tailed Kruskal–Wallis test). **e**, Representative tracings of CA1 pyramidal neurons from DNRAb$^-$ and DNRAb$^+$ LAIR-1 cKO mice treated

with saline or captopril. **f**, Captopril treatment had no effect on dendritic complexity in LAIR-1 cKO DNRAb^{-} ($P > 0.99$) and DNRAb^{+} ($P = 0.88$) mice treated with either saline or captopril (5 mg kg^{-1}; mean ± s.e.m.; $n = 2$–3 mice per group; $n = 19$–27 neurons analyzed per group; two-tailed, linear mixed model test with Tukey's adjustment).

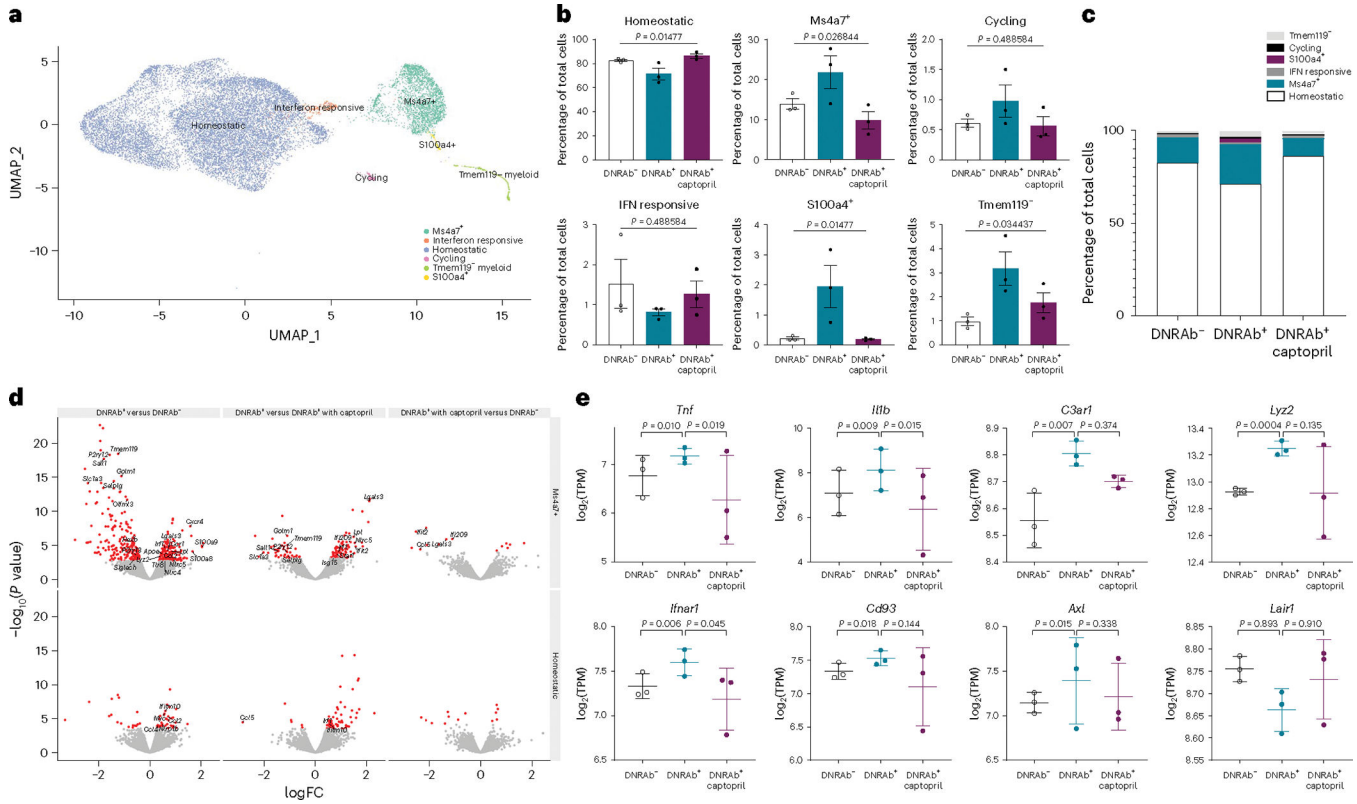

Fig. 4 |. Hippocampal microglial scRNA-seq shows that ACE inhibitors mitigate DNRAb phenotype.

a, UMAP plot of single-cell microglia data, with each cell colored by microglia cluster: cycling (pink), homeostatic (blue), IFN responsive (orange), Ms4a7^{+} (green), S100a4^{+} (yellow) and Tmem119^{-} (light green). **b**, Cell-type composition plots. The percentage of total cells is represented in each cluster in DNRAb^{-}, DNRAb^{+} and captopril-treated DNRAb^{+} B6.H2^{d} mice (mean ± s.e.m.; $n = 3$ mice per group; two-tailed ANOVA, false discovery rate (FDR)-adjusted P values shown: $P = 0.01477$ (homeostatic), $P = 0.026844$ (Ms4a7^{+}), $P = 0.488584$ (cycling), $P = 0.488584$ (IFN responsive), $P = 0.01477$ (S100a7^{+}) and $P = 0.034437$ (Tmem119^{-})). **c**, Stacked bar plots of the cell-type composition in each condition. **d**, Volcano plots of the differentially expressed genes comparing between different conditions (columns) in Ms4a7^{+} and homeostatic microglia (rows). The y axis is $\log_{10}(P \text{ value})$, the x axis is the log(fold-change) (log(FC)) reported by EdgeR. Genes with FDR < 0.05 are colored red and genes of interest are labeled. **e**, Expression of genes of interest in different conditions in Ms4a7^{+} microglia. Pseudobulk expression levels are calculated on a per-mouse basis (y axis, $\log_2$(transcripts per million) ($\log_2$(TPM))), stratified by condition (mean ± s.d.; two-tailed FDR; P values are uncorrected).

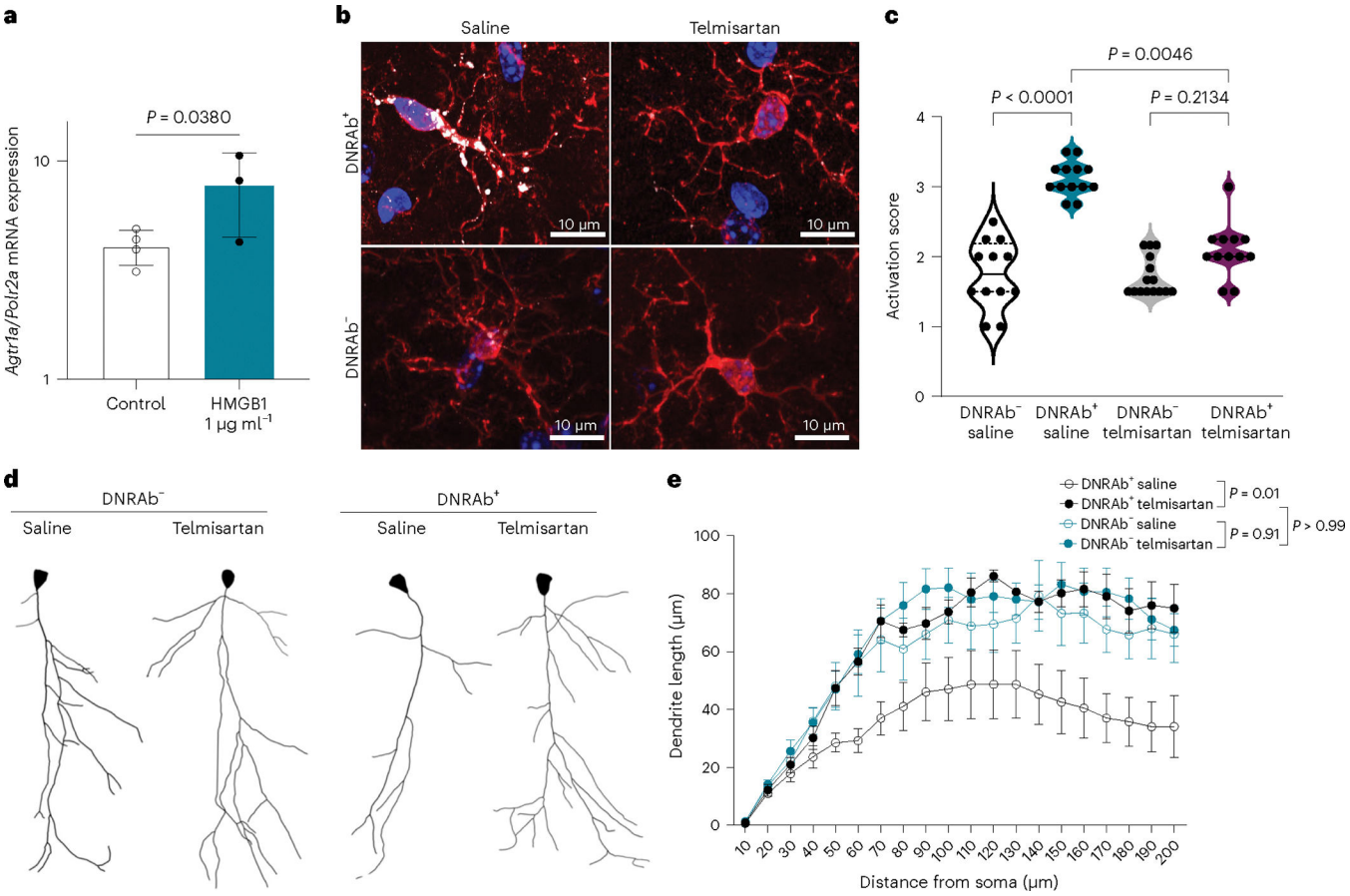

Fig. 5 |. ARB replicates effects of ACE inhibitors on neurons and microglia.

a, Increased *Agtr1a* mRNA expression in microglia stimulated with 1 μg ml^{-1} of HMGB1 compared with microglia cultured in medium for 6 h (mean ± s.d.; ex vivo microglia isolated from three to four B6 mice; one-tailed, unpaired Student's *t*-test: $P = 0.0380$). **b**, Representative sections of microglia in CA1 stratum radiatum stained for Iba1 (red) and CD68 (white) in $DNRAb^+$ (top) and $DNRAb^-$ (bottom) Balb/c mice treated with saline (left) or telmisartan (right, 1 mg kg^{-1}; $n = 2–3$ mice per group). **c**, Decreased activation score in $DNRAb^+$ microglia in Balb/c mice treated with telmisartan compared with saline-treated counterparts ($P = 0.0046$) based on morphology and CD68 expression (median (solid line) with quartiles (dash); $n = 2–3$ mice per group; $n = 10–15$ microglia scored per mouse; two-tailed Kruskal–Wallis test). **d**, Representative tracings of CA1 pyramidal neurons from $DNRAb^-$ and $DNRAb^+$ Balb/c mice treated with saline or telmisartan. **e**, Telmisartan treatment rescued dendritic complexity in $DNRAb^+$ Balb/c mice compared with saline-treated counterparts (mean ± s.e.m.; $n = 5–6$ mice per group; $n = 2–18$ neurons analyzed per mouse; two-tailed, linear mixed model test with Tukey's adjustment: $P = 0.01$).

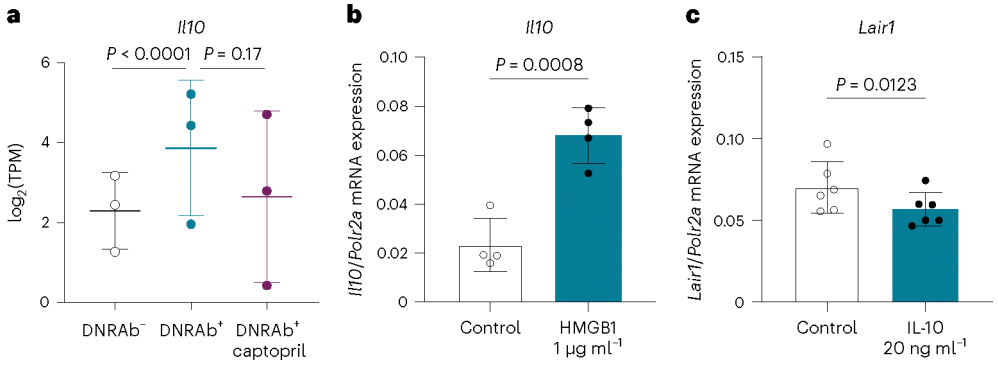

Fig. 6 |. IL-10 is induced by HMGB1 and suppresses *Lair1* expression.

a, *Il10* expression is higher in B6.H2^{d} DNRAb^{+} mice than in DNRAb^{-} mice in Ms4a7^{+} hippocampal microglia ($P < 0.0001$). Pseudobulk expression levels are calculated on a per-mouse basis (*y* axis, $\log_2$(TPM)), stratified by condition (mean ± s.d.; two-tailed FDR; *P* values uncorrected). **b**, Increased *Il10* mRNA expression in microglia stimulated with 1 μg ml^{-1} of HMGB1 compared with unstimulated microglia cultured in medium for 6 h (mean ± s.d.; ex vivo microglia isolated from four WT (B6) mice; two-tailed, paired Student's *t*-test: $P = 0.0008$). **c**, Decreased *Lair1* mRNA expression in microglia stimulated with 20 ng ml^{-1} of IL-10 compared with unstimulated microglia cultured in medium for 6 h (mean ± s.d.; ex vivo microglia isolated from 6 WT (B6) mice; two-tailed, paired Student's *t*-test: $P = 0.0123$).

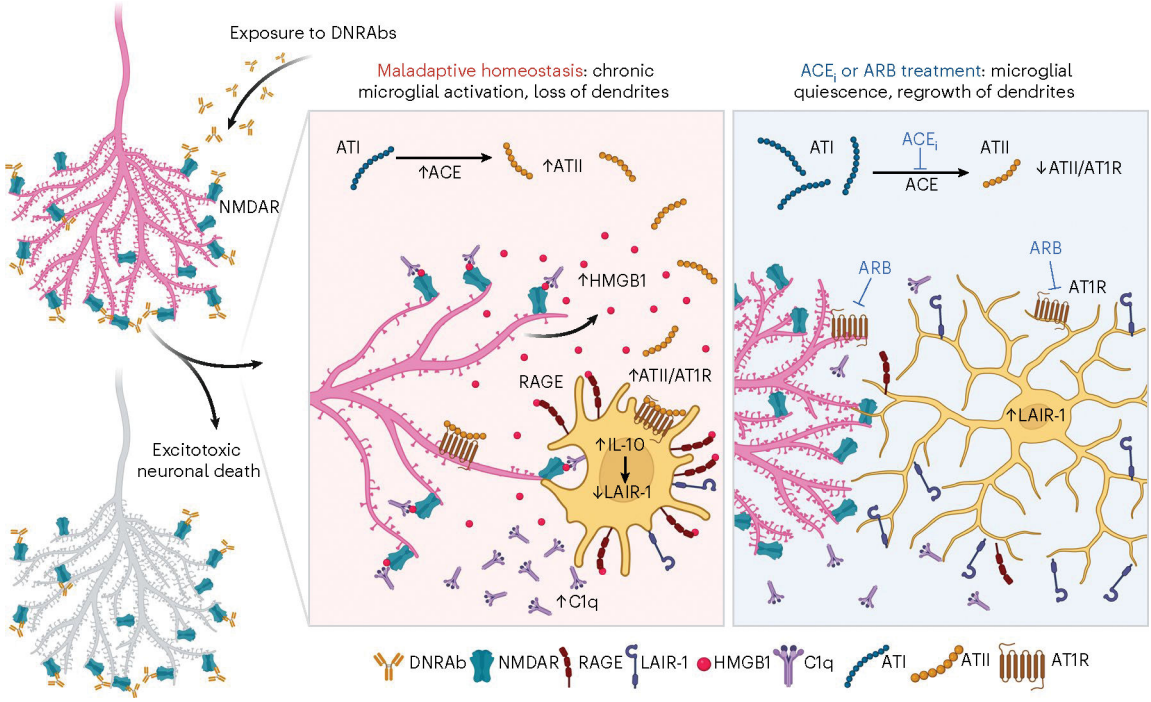

Fig. 7 |. Outcomes of DNRAb-mediated neuronal damage.

Exposure of hippocampal CA1 pyramidal neurons to DNRAbs results in DNRAb binding to NMDARs, mediating excitotoxic death in 20–30% of neurons. A maladaptive equilibrium begins as a microglial response to apoptotic neuronal debris and progresses as stressed neurons secrete HMGB1, which activate microglia by binding RAGE. Activated microglia secrete proinflammatory cytokines, type I IFN, C1q and IL-10 in response to HMGB1. IL-10 suppresses LAIR-1 expression on microglia. The secreted HMGB1 acts as a bridge by binding both synaptic proteins and C1q, which tags synapses for microglia-dependent synapse loss, resulting in a loss of neuronal dendrite branching and spine density. Captopril or telmisartan treatment decreases the proinflammatory ATII/AT1R ligation by inhibiting ACE, which converts ATI to ATII, or blocking AT1R, respectively. This allows for microglial LAIR-1 upregulation and quiescence, the return to a healthy homeostasis and regrowth of dendritic branches and spines. ACE_i, ACE inhibitor. Image created with Biorender.com.